Near-Inertial Internal Waves and Sea Ice in the Beaufort Sea

Citation	Martini, K. I., Simmons, H. L., Stoudt, C. A., & Hutchings, J. K. (2014). Near-Inertial Internal Waves and Sea Ice in the Beaufort Sea. Journal of Physical Oceanography, 44(8), 2212-2234. doi:10.1175/JPO-D-13-0160.1
DOI	10.1175/JPO-D-13-0160.1
Publisher	American Meteorological Society
Version	Version of Record
Terms of Use	http://cdss.library.oregonstate.edu/sa-termsofuse

Near-Inertial Internal Waves and Sea Ice in the Beaufort Sea*

KIM I. MARTINI

Joint Institute for the Study of the Atmosphere and Oceans, University of Washington, and NOAA/Pacific Marine Environmental Laboratory, Seattle, Washington

HARPER L. SIMMONS AND CHASE A. STOUDT

School of Fisheries and Ocean Sciences, University of Alaska Fairbanks, Fairbanks, Alaska

JENNIFER K. HUTCHINGS

Oregon State University, Corvallis, Oregon

(Manuscript received 16 July 2013, in final form 20 May 2014)

ABSTRACT

The evolution of the near-inertial internal wavefield from ice-free summertime conditions to ice-covered wintertime conditions is examined using data from a yearlong deployment of six moorings on the Beaufort continental slope from August 2008 to August 2009. When ice is absent, from July to October, energy is efficiently transferred from the atmosphere to the ocean, generating near-inertial internal waves. When ice is present, from November to June, storms also cause near-inertial oscillations in the ice and mixed layer, but kinetic energy is weaker and oscillations are quickly damped. Damping is dependent on ice pack strength and morphology. Decay scales are longer in early winter (November–January) when the new ice pack is weaker and more mobile, decreasing in late winter (February–June) when the ice pack is stronger and more rigid. Efficiency is also reduced, as comparisons of atmospheric energy available for internal wave generation to mixed layer kinetic energies indicate that a smaller percentage of atmospheric energy is transferred to near-inertial motions when ice concentrations are >90%. However, large kinetic energies and shears are observed during an event on 16 December and spectral energy is elevated above Garrett–Munk levels, coinciding with the largest energy flux predicted during the deployment. A significant amount of near-inertial energy is episodically transferred to the internal wave band from the atmosphere even when the ocean is ice covered; however, damping by ice and less efficient energy transfer still leads to low Arctic internal wave energy in the near-inertial band. Increased kinetic energy below 300 m when ice is forming suggests some events may generate internal waves that radiate into the Arctic Ocean interior.

1. Introduction

The Arctic internal wavefield is relatively weak when compared to nonpolar seas. This is due to weak tides (Kowalik and Proshutinsky 1994; Padman and Erofeeva 2004) and the damping and insulating effects of sea ice on internal wave generation by winds (Levine et al. 1985; Morison et al. 1985). Winds generate near-inertial internal waves throughout the year (D'Asaro and Morehead 1991; Halle and Pinkel 2003; McPhee 1978; Pinkel 2005), but their strength is heavily modulated by the absence or presence of sea ice. Recent work by Rainville and Woodgate (2009) suggests internal wave generation has a strong seasonal cycle in the Arctic, but it remains unclear how seasonal changes in wind forcing and ice dynamics affect the internal wavefield. It is in the context of the annual cycle of sea ice growth and retreat that the modification of the near-inertial internal wavefield by ice is examined using observations from a yearlong moored array on the Beaufort continental slope from August 2008 to August 2009.

* Pacific Marine Environmental Laboratory Contribution Number 4127 and Joint Institute for the Study of the Atmosphere and Ocean Contribution Number 2208.

Corresponding author address: Kim I. Martini, Joint Institute for the Study of the Atmosphere and Oceans, University of Washington, 3737 Brooklyn Ave. NE, Box 355672, Seattle, WA 98195-5672.
E-mail: kmartini@uw.edu

DOI: 10.1175/JPO-D-13-0160.1

When ice is present during the winter, the strength of the internal wavefield is significantly reduced. Vertical displacement spectra obtained near the 1000-m isobath north of the Yermak Plateau (Levine et al. 1985) and over the deep Beaufort Sea during the Arctic Internal Wave Experiment (AIWEX) (Levine et al. 1987; Levine 1990) show internal wave energies under drifting pack ice are nearly an order of magnitude smaller than subpolar open-ocean values. Internal wave shear levels are also low over the Arctic abyssal plains, but increase over the rougher topography possibly due to increased internal tide generation (D'Asaro and Morison 1992). Sea ice also may dissipate internal wave energy by altering the surface boundary condition. Increased drag at the ice–ocean interface causes an oscillating boundary condition that acts as a sink for internal wave energy and could account for the low internal wave energy levels in the Arctic (Morison et al. 1985; D'Asaro and Morison 1992).

When ice is absent during the summer, the strength of the internal wavefield increases. Rainville and Woodgate (2009) found that near-inertial shear and kinetic energy increase when the shallow Chukchi Sea (depths < 110 m) is ice-free from July to October and is nearly absent when ice covered from November to June. Strong atmospheric storms occur during the winter, but near-inertial ocean velocities are small and have no apparent relationship to wind strength. During the summer, near-inertial shear increases in response to wind stress, suggesting that when ice is absent, the ocean is no longer insulated from atmospheric forcing, allowing for the generation of internal waves. Similarly, Plueddemann et al. (1998) observed a seasonal cycle in near-inertial oscillations of buoys frozen into pack ice that drifted from the Chukchi Plateau into the Beaufort Sea. The seasonal cycle of wind-generated near-inertial motions is reversed from the seasonal cycle of wind forcing in the Beaufort and Chukchi Seas, where winds are strongest during winter and weakest during summer [National Centers for Environmental Prediction (NCEP) reanalysis data provided by the National Oceanic and Atmospheric Administration (NOAA)/Office of Oceanic and Atmospheric Research (OAR)/Earth System Research Laboratory/Physical Sciences Division (ESRL PSD), Boulder, Colorado, from their website at http://www.esrl.noaa.gov/psd/]. This is in contrast to the ice-free ocean, where energy in the near-inertial band not only increases in response to storms, but also has a seasonal cycle that corresponds to the seasonal cycle of wind forcing (Alford and Whitmont 2007).

In contrast to observations by Rainville and Woodgate (2009), intermittent increases in internal wave energy occur during the ice-covered season in the deeper Beaufort Sea (depths > 1000 m), predominantly in the near-inertial frequency band and are associated with atmospheric storms and ice deformation (Halle and Pinkel 2003; Pinkel 2005). However, not all storms in the Beaufort Sea cause a near-inertial response, and it is unclear whether coincident ice deformation allows or is caused by an increase in near-inertial wave energy. The differences in the wintertime near-inertial response between the Beaufort and Chukchi Seas suggest that near-inertial internal wave generation is not only seasonally dependent, but spatially dependent as well and may be due to regional changes in wind forcing, ice pack strength, or mixed layer depth.

The effect of the ice pack on internal wave generation and the evolution of the near-inertial internal wavefield from ice-free to ice-covered conditions on the Beaufort continental slope are examined here. It will be shown that the mechanisms by which internal waves are generated by winds when ice is present or absent are similar, but the ocean response to wind forcing is modified by ice. The ice–ocean response is compared to atmospheric forcing, comparing ice-covered and ice-free periods, and the effect of ice pack strength and mobility on the near-inertial response is also discussed. This manuscript focuses on the near-inertial band, but where feasible, characteristics of the entire internal wave band are explored by looking at vertical wavenumber and frequency spectra.

2. Methods

a. *Moorings*

As part of the Ice Covered Oceanic Response to Atmospheric Storms project (ICORTAS), a triangular array of three moorings, I1, I2, and I3, were deployed from August 2008 to August 2009 on the Beaufort continental slope spaced 10.5 km apart at the 1266-, 1666-, and 1886-m isobaths, respectively (Fig. 1). Two moorings, BS3 and BS4, were deployed by the Woods Hole Oceanographic Institution on the continental shelf at the 100- and 500-m isobaths with upward-looking ADCPs to measure surface velocities, detailed in Schulze and Pickart (2012). Mooring BS3 was also deployed with an Arctic winch to obtain daily CTD profiles from 0 to 40 m (data courtesy of R. Pickart, Woods Hole Oceanographic Institution, 2009). The Arctic winch is a buoyant sensor suite containing a winch and CTD attached to the top float of the mooring with a nylon line [described in more detail in Pickart et al. (2013a,b) and Weingartner et al. (2010)]. The sensor suite floats from its resting position on subsurface flotation at 40 m to the surface to obtain an upper-ocean CTD profile. The sensor suite is then winched back down once its vertical motion has stopped, either at the sea surface or underneath the ice. Data from mooring A1 on the shelf edge at Barrow Canyon were provided by S. Okkonen (2009,

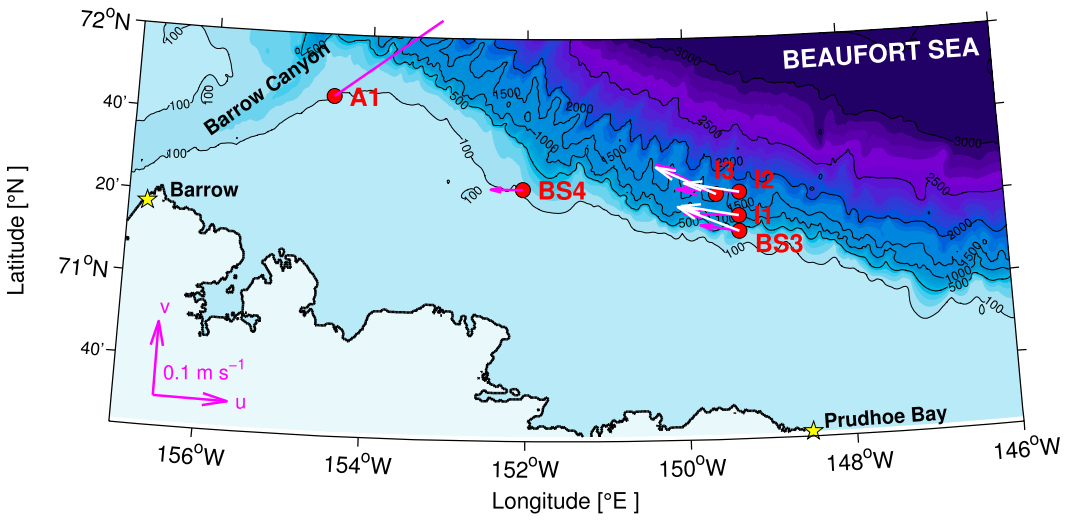

FIG. 1. Bathymetric map of the Beaufort Sea continental slope and moorings (labeled red circles). Arrows show average water velocities between 10 and 20 m (magenta) and surface ice velocities (white) from yearlong ADCP records. Mean currents at A1 (off the map) near Barrow Canyon are larger (0.3 m s^{-1}) than at other moorings (<0.1 m s^{-1}).

unpublished data). The observation dates and depths for each instrument are listed in Table 1. Each mooring in the triad was deployed with a McLane moored profiler (MMP) to obtain 3-h profiles of horizontal velocity, pressure, conductivity, and temperature from 100 to 600 m in 2-m bins [47% of the Wentzel–Kramers–Brillouin (WKB) stretched water depth at I3 (Leaman and Sanford 1975)] and an upward-looking RDI 300-kHz Workhorse ADCP sampling every 8 min to capture horizontal velocities above the range of the MMP in 4-m bins (25%–35% of the WKB stretched water depth) (Fig. 2). The MMP samples at a rate of 1 Hz, crawling at a speed of 0.25 m s^{-1} for an effective resolution of 25 cm before binning. The MMP on mooring I1 had a severe compass error so velocities could not be determined, and no data were obtained from the MMP on moorings I2 due to a corrupt memory card. The MMP at I3 was the only instrument to measure currents below 100-m, although it did not resolve the full-seasonal cycle of near-inertial currents because it stopped sampling on 3 December 2008 when the battery died. Only on mooring I2 was the ADCP deployed deep enough (8–100 m) to measure horizontal velocities and vertical shear in the stratified interior below the mixed layer for the entire year. The ADCP at mooring A1 stopped sampling on 13 December 2008.

Zonal and meridional velocity data from the ADCP are vertically interpolated onto a higher-resolution constant depth grid with 1-m spacing to reduce interpolation errors when moorings are blown down by strong currents (Fig. 2). All statistics except for shear are calculated from the interpolated data. The accuracy of uninterpolated 8-min ADCP velocities is highly sensitive to the scatterer density. A lack of scatters leads to velocity errors up to 1 cm s^{-1}, larger than the standard ADCP velocity error

TABLE 1. Inventory of moorings deployed as part of the ICORTAS experiment. Data types are abbreviated as horizontal velocities u, v, temperature T, conductivity C, and pressure P.

Mooring	Lat (°N)	Lon (°W)	Water depth (m)	Instrument	Start date	End date	Deployment depth (m)	Data type
A1	71.75	−154.48	100	ADCP	9 Aug 2008	13 Dec 2008[a]	0–80	u, v
B3	71.22	−149.33	500	ADCP	7 Aug 2008	1 Aug 2009	4–35	u, v
I1	71.28	−149.33	1266	ADCP	11 Aug 2008	30 Jul 2009	8–60	u, v
				MMP	11 Aug 2008[b]		80–600	T, C, P
I2	71.38	−149.32	1666	ADCP	11 Aug 2008	31 Jul 2009	8–100	u, v
				MMP	11 Aug 2008[c]		80–600	
I3	71.37	−152.05	1886	ADCP	12 Aug 2008	31 Jul 2009	7–58	u, v
				MMP	15 Aug 2008	12 Mar 2008	90–580	u, v, T, C, P

[a] Stopped sampling early in December.
[b] Unable to obtain velocities due to a severe compass error.
[c] Corrupt memory card, no data obtained.

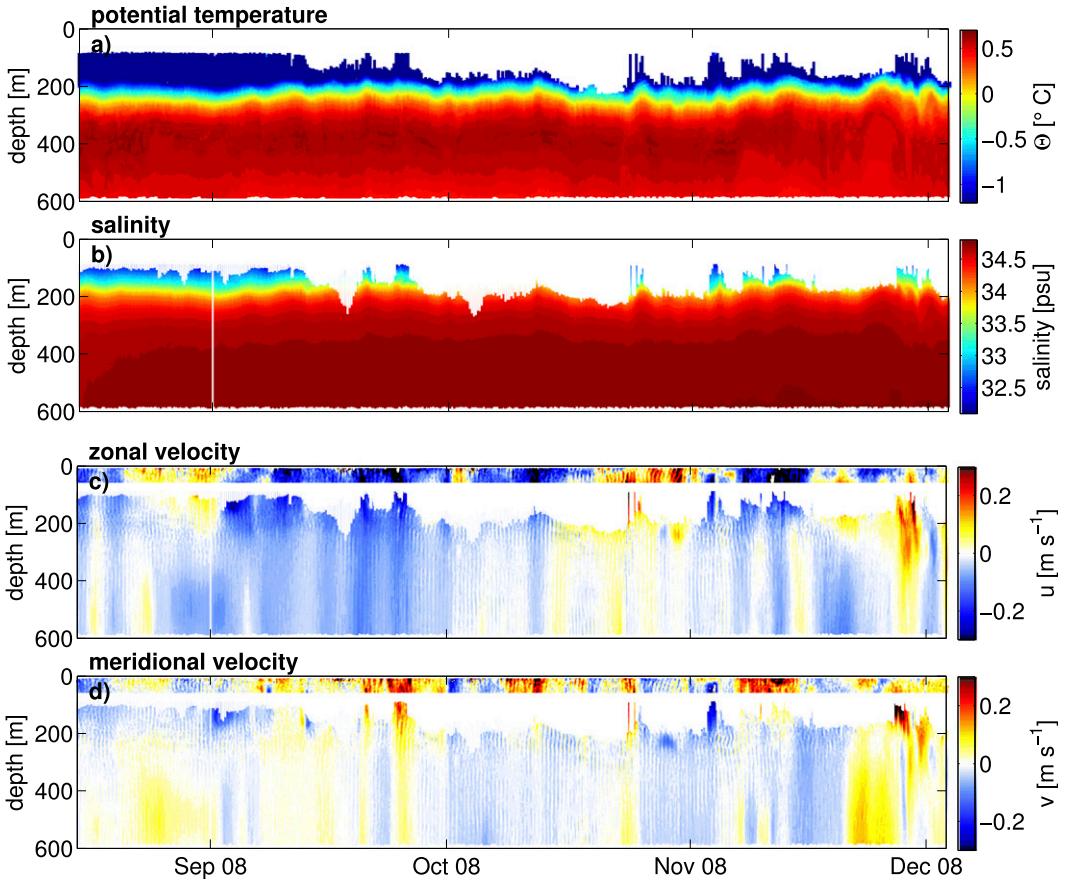

FIG. 2. MMP and ADCP data at mooring I3. (a) Potential temperature and (b) salinity are from the CTD deployed on the MMP. (c) Zonal and (d) meridional velocities from both the ADCP and the MMP. The 8-min ADCP data have been binned onto a 1-m constant depth grid. The MMP starts an up or down profile every 3 h and has been binned onto a 2-m grid.

of $\pm 0.5\,\mathrm{cm\,s^{-1}}$. This is the same order of magnitude of velocity differences between adjacent bins and can lead to large errors in vertical shears, but not for velocity itself that is typically 10–20 times larger than the error. The effect of scatterer density on estimating shear is apparent during spring and fall, when vertical shear magnitudes have a strong diurnal cycle directly correlated to the daily vertical migration of zooplankton into the range of the ADCP. The diurnal cycle disappears during summer and winter when diurnal vertical migration no longer occurs due to 24-h light and darkness, respectively. Therefore, before calculating shear, raw 4-m ADCP velocities are averaged into 1-h bins to reduce noise and errors associated with the fluctuating density of scatterers.

Vertical wavenumber spectra are calculated from the WKB stretched and scaled moored profiler horizontal velocities from 275 to 575 m. Each profile takes approximately 30 min to complete; the mean buoyancy frequency N is approximately 35 min (1.7 cph), indicating that high-frequency internal waves undergo nearly one complete oscillation during each profile. To minimize aliasing at the highest internal wave frequencies, vertical wavenumber spectra are calculated over 27-m chunks corresponding to a profiling time of approximately 1.7 min or one quarter of the maximum buoyancy period.

Mixed layer depth is estimated from daily Arctic winch near-surface CTD profiles at BS3 at the 500-m isobath (Fig. 3). The bottom of the mixed layer is defined to be where the difference in density from the surface density is greater than a predefined threshold, empirically determined here to be $0.05\,\mathrm{kg\,m^{-3}}$. The mixed layer has a strong seasonal cycle, deepening in winter due to convection caused by brine rejection during seasonal ice formation.

b. *Near-inertial signal*

To discriminate motions at different time scales, the observations are partitioned into high-, low-, and near-inertial frequency bands. High frequencies are >10 cycles per day (cpd), corresponding to a period of

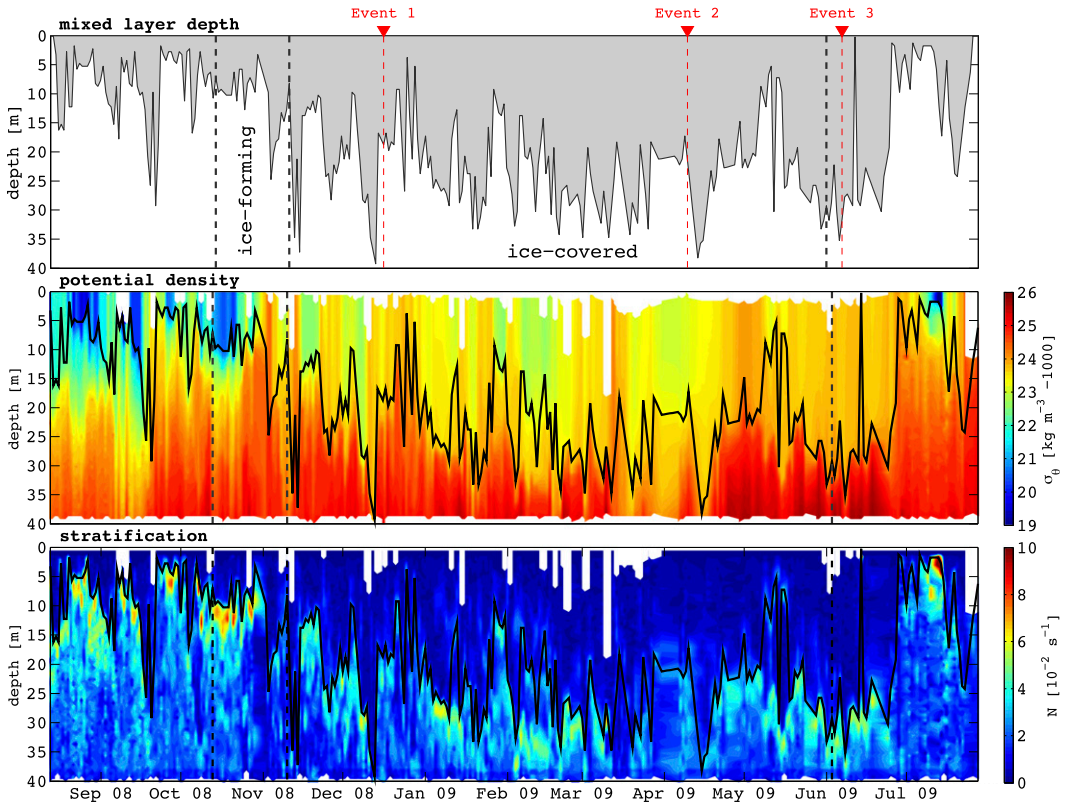

FIG. 3. Arctic winch CTD data (courtesy of R. Pickart) at the shelf break are used to find (top) mixed layer depth from changes in (middle) potential density. (bottom) Stratification is at a maximum immediately below the base of the mixed layer.

2.4 h and low frequencies are <0.3 cpd with a period of 3 days. The near-inertial band is narrow, ranging from the local inertial frequency at 71.5°N, 1.9 cpd, to the local inertial frequency at 90°N, 2.00 cpd.

Near-inertial velocities are extracted using sliding harmonic fits at the local inertial frequency f_{local} on zonal and meridional velocity components to resolve the temporal evolution of the near-inertial response for events occurring at 2–3-day time scales following Martini et al. (2011). Spectral analysis of ADCP velocity data shows there is a narrow spectral peak at the local inertial frequency (Fig. 4), but harmonic fits are employed rather than filtering because the MMP does not sample at a constant rate and this method better resolves individual near-inertial events. At the moorings (latitude = 71.5°N), the local inertial frequency corresponds to a 12.63 h inertial period. At each MMP depth, a cosine that is three inertial periods long (37.89 h) with frequency $f_{71.5°\text{N}}$ is slid along in time and fit to the data at 1.5-h intervals. A 0.5-day-long cosine fit at 1.5-h intervals is used on the ADCP because the sampling rate is higher.

Because of the short window length, the harmonic fit cannot distinguish signals with 9.5- to 19.0-h periods from inertial signals. The windowed fits contain contributions from a broader bandwidth than just the inertial frequency, including the 12.42-h M_2 and the 12-h S_2 semidiurnal tides. Therefore, it can be difficult to distinguish wind-generated near-inertial oscillations from semidiurnal tides. Tidal velocity is estimated from ADCP and MMP data by fitting semidiurnal tidal constituents to the entire data record. Fitted tidal velocities are somewhat smaller than Arctic tidal models, having maximum semidiurnal velocities of 0.01 and 0.02 m s^{-1} (Kowalik and Proshutinsky 1994; Padman and Erofeeva 2004), respectively. These are smaller than near-inertial velocities obtained with the windowed fits, which typically range from 0.05 to 0.2 m s^{-1}, suggesting the majority of velocity variance in the near-inertial band is wind generated rather than tidally generated and are not subtracted from the semidiurnal fits. Near-inertial velocities lack a spring–neap cycle, which should be easily observed during winter when the generation of internal waves by wind is weak, suggesting surface tides and topographically generated internal tides are weak. Near-inertial horizontal kinetic energy (HKE) is typically 5%–20% of the total HKE, where most of the energy is subinertial.

Wind-generated oscillations rotate anticyclonically with time and can be further isolated by separating

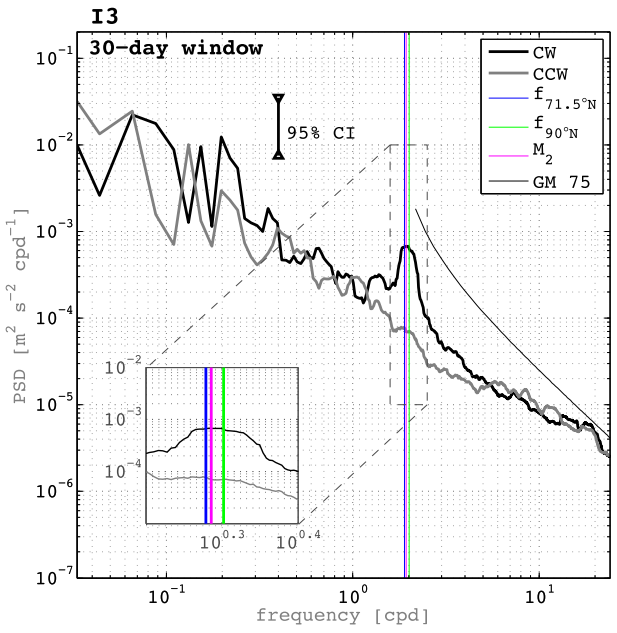

FIG. 4. Spectra of ADCP currents from 7 to 58 m that rotate clockwise (black) and counterclockwise (gray) with time. The data were divided into 30-day chunks and spectra were depth averaged. The 95% confidence interval is shown by the black vertical bar. The clockwise rotating spectra have a broad peak that spans the local inertial frequency $f_{71.5N°}$, the semidiurnal M_2 frequency, and the inertial frequency at the North Pole $f_{90°N}$ (inset).

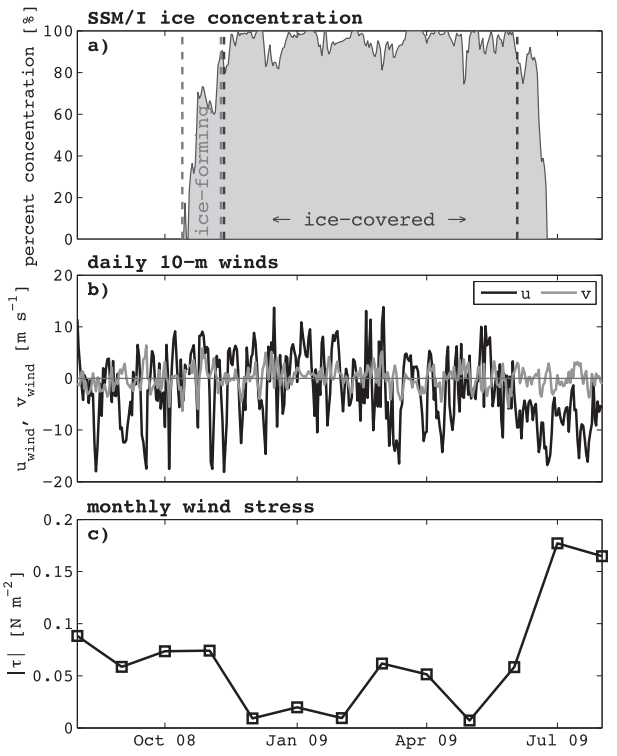

FIG. 5. (a) SSM/I satellite ice concentrations from the pixel closest to the moored array. Ice-forming (13 Oct–10 Nov, percent concentration $< 90\%$) and ice-covered (10 Nov–3 Jun, percent concentration $> 90\%$) periods are noted. (b) Daily averaged winds from Prudhoe Bay at 10-m above ground. (c) Monthly averaged wind stress magnitude at Prudhoe Bay.

horizontal velocities into clockwise and anticlockwise rotating components (Leaman and Sanford 1975). Clockwise rotating velocities in the near-inertial band may be wind-generated, while counterclockwise rotating velocities are not. Only the clockwise rotating component has a near-inertial peak, suggesting that semidiurnal oscillations are predominantly wind generated (Fig. 4). Shear spectra taken below the mixed layer are similar, where only the clockwise rotating component of shear has a peak at the local inertial frequency (not shown).

c. Ice coverage and velocities

Mesoscale ice concentrations are obtained from Special Sensor Microwave Imager (SSM/I) satellite data (Comiso 2012). The spatial resolution of the SSM/I data is $25 \times 25\,\text{km}^2$, and ice concentrations come from the pixel closest to each mooring. The region over the moorings is determined to be ice free when SSM/I concentrations are 0%, ice covered above 90%, and ice forming when between 0% and 90% in the fall (Fig. 5). Ice velocity is calculated by the upward-looking ADCPs using the bottom-tracking mode at each mooring, sampling every 8 min. Ice detection is verified from ADCP error velocities following Shcherbina et al. (2005). To detect ice, all four ADCP beams must reflect from solid ice; therefore, only ice fragments larger than the horizontal footprint of the beams can be detected, which is ~30 m when deployed at a depth of 80 m. Younger, thinner, and therefore more fragmented ice may not be detected.

By the end of summer 2009, ice less than 5 yr old had melted out completely in the western Beaufort, suggesting that the ice pack over the moorings is generally younger and thinner than in the rest of the Beaufort (Hutchings and Rigor 2012). However, in mid-January, ice-tethered profilers, deployed as part of the International Arctic Buoy Program (IADP) pass within 50 km of the moored array. They are deployed on multiyear ice that drifted clockwise in the Beaufort Gyre, to the north of the moorings, suggesting that older, thicker, and stronger ice may occasionally cover the moorings.

Similar to the ADCP, ice velocities are separated into clockwise and counterclockwise rotating components and near-inertial band velocities extracted by employing sliding harmonic fits at the local inertial frequency. Ice near-inertial horizontal kinetic energy $\text{HKE}_{\text{ice}}^{\text{CW}}$ is found by $\text{HKE}_{\text{ice}}^{\text{CW}} = 0.5\rho_{\text{ice}}\langle u_{\text{ice}}^2 + v_{\text{ice}}^2\rangle_t$, where ρ_{ice} is the density of ice, u_{ice} and v_{ice} are the near-inertial zonal/meridional ice velocities, and $\langle\rangle_t$ is the time average over an inertial period.

To investigate ice pack mobility and how it relates to atmospheric forcing, ice divergence and maximum shear strain rates are calculated following Hutchings et al. (2012). Divergence and the maximum shear strain rate of ice are determined from the raw, unfiltered ice velocities at the three slope moorings: I1, I2, and I3. Ice divergence is

$$\epsilon_I = \nabla \cdot u_{\text{ice}} = \frac{\partial u_{\text{ice}}}{\partial y} + \frac{\partial v_{\text{ice}}}{\partial x}, \quad (1)$$

and maximum shear strain rate is

$$\epsilon_{II} = \frac{1}{2}\sqrt{\left(\frac{\partial u_{\text{ice}}}{\partial x} - \frac{\partial v_{\text{ice}}}{\partial y}\right)^2 + \left(\frac{\partial u_{\text{ice}}}{\partial y} + \frac{\partial v_{\text{ice}}}{\partial x}\right)^2}, \quad (2)$$

where u_{ice} and v_{ice} are the observed meridional and zonal ice velocities, respectively, and dx and dy are the meridional and zonal distances between the moorings. Positive ice divergences indicate an expanding ice pack, and negative divergences indicate a contracting ice pack. Maximum shear strain rates are used because it indicates whether ice is moving together as one rigid sheet (small ϵ_{II}) or independently in smaller sections (large ϵ_{II}) over the spatial scale of three moorings.

Near-inertial and low-passed ice velocities are also compared to qualitatively determine whether the entire ice pack is moving together over the moorings (10.4-, 10.5-, and 13.9-km separation distances) at shorter (12.65 h) and/or longer (>3 days) time scales during near-inertial events. The wind factor $|u_{\text{ice}}|/|u_{\text{wind}}|$, the ratio of ice speed to wind speed, is also calculated, which directly compares the ice response to wind forcing. When the wind factor is larger, it indicates the ice is pushed harder by the wind. The wind factor is derived from the "Nansen–Ekman" ice-drift law (Ekman 1902; Nansen 1902), which found that freely drifting ice speeds are about 2% of the geostrophic wind speed, corresponding to a wind factor of 0.02. Observations from buoys suggest the wind factor is smaller in the central Arctic and are 0.008% or 0.8% (Thorndike and Colony 1982). Here, observed wind factors are typically larger, ranging from 0.01 to 0.1, likely due to the influence of ocean currents on ice-drift speed.

d. Wind data

The transfer of momentum from the atmosphere to the ice–ocean system at the moorings is quantified by calculating wind stress from 6-min NOAA ocean buoy wind data at Prudhoe Bay, Alaska, the closest station to the moored array (~100 km to the southeast), using the Large and Pond (1981) formulation. Wind speed and direction is sampled every 6 min, then transformed into Cartesian coordinates and averaged into 1-h bins. Remote wind data are used in the slab model presented in section 3f because the temporal resolution of reanalysis wind products (3-h resolution) is too coarse to produce accurate predictions as discussed in the appendix.

3. Observations and discussion

In the following sections, the modification of near-inertial band mixed layer oscillations and internal waves by sea ice will be discussed. Briefly, the near-inertial internal wavefield has a seasonal cycle dictated by the presence or absence of sea ice. This is best seen in kinetic energy and vertical shear, which are both large when the Beaufort continental slope is ice free and small when ice covered. However, during the winter there are bursts of energy in the near-inertial band that suggests that in favorable conditions, internal waves can still be generated by winds even when ice is present. The characteristics of background ocean variability, sea ice, and the seasonal cycle of the near-inertial response are presented following a discussion of how sea ice modifies the response to wind forcing.

a. Background low-frequency currents

At the slope moorings, I1-I3 and BS3, surface velocities and ice drift are predominantly to the northwest, driven by the anticyclonic Beaufort Gyre (Fig. 1). Low-frequency horizontal velocities (low-passed with a 3-day cutoff) are largest (0.2–0.5 m s^{-1}) and nearly uniform between 0 and 200 m. Below 200 m, the currents weaken and are often incoherent with surface velocities. Occasionally, velocities switch to the southeast for 5–10-day periods. The reversals may be attributed to offshore meanders of an eastward jet that follows the shelf break (originating at Point Barrow and fed by the Alaska Coastal Current) or anticyclonic eddies shed from the jet (Spall et al. 2008). At mooring A1, located on the Barrow Canyon slope, mean water velocities are directed offshore to the northwest due to the same Point Barrow jet.

b. Sea ice characteristics

The moorings on the slope are nearly completely ice covered (mean concentrations are >90%) from 10 November to 3 June (Fig. 5). Periods of open water occur during this time as occasionally ice is not detected over the moorings and is usually coincident with decreased SSM/I ice concentrations. Average open-water periods last 1 h, but can persist as long as 25 h. Freeze up, when

TABLE 2. Nonparametric Kendall rank correlation coefficients Γ between daily averages of ice near-inertial HKE, SSM/I percent ice cover, maximum ice shear–strain rate, and low-frequency ice speed during the ice-covered period from 10 Nov to 3 Jun. Kendall rank correlation coefficients are used rather than Pearson's rank correlation to detect nonlinear relationships between the variables (which Pearson's cannot), since they are highly skewed and nonnormal due to complex ice mechanics (Kendall 1938).

Γ	HKE_{ice}^{CW} ($J\,m^{-2}$)	Ice cover (%)	ϵ_{II} $(s^{-1})^1$	$\lvert u_{ice}\rvert$ ($m\,s^{-1}$)
HKE_{ice}^{CW}	1	−0.47	0.55	0.53
% ice cover	−0.47	1	−0.42	−0.37
ϵ_{II}	0.55	−0.42	1	0.62
$\lvert u_{ice}\rvert$	0.53	−0.37	0.62	1

the majority of ice is formed, lasts from 13 October to 10 November, and ice during this period is usually characterized as being thinner and more mobile. The moored observations agree with the characterization of a looser ice pack during the ice-forming period as ice velocities are higher and there is more open water (ice concentrations range from 0% to 80%) than during the ice-covered season (where ice concentrations are above 80%).

Throughout the winter, the ice pack becomes stronger as it thickens through thermodynamic growth, but its strength is very sensitive to nearby open-water concentrations (Rothrock 1975). During the ice-covered season starting 10 November, near-inertial kinetic energy of ice (HKE_{ice}^{CW}) is negatively correlated with ice cover (Table 2). Maximum shear strain rates and low-frequency ice speeds are positively correlated with HKE_{ice}^{CW}, suggesting a mobile and fragmented ice pack allows near-inertial oscillations.

c. Vertical wavenumber spectra

Vertical wavenumber spectra obtained from MMP profiles of horizontal velocities are used to examine internal wave energy and wavenumber content. The observations from the ICORTAS moorings are compared to historical spectra from AIWEX (D'Asaro and Morison 1992) and the Garrett–Munk (GM75) model (Garrett and Munk 1975) here, but the differences will be discussed in more detail in section 3i.

The GM75 model (Garrett and Munk 1975) is a description of the internal wavefield in frequency space as a function of the characteristic energy E_0 and the vertical wavenumber scale j_*. By minimizing the variance between the vertical wavenumber spectra and GM75 model, the best fit to the observations is obtained by setting the energy level to $E_0 = 5.4 \times 10^{-6}$ and vertical wavenumber scale to $j_* = 25$ (expressed here as vertical mode number) (Fig. 6). During ICORTAS, mean spectral energy levels are only ~1.5 times larger than

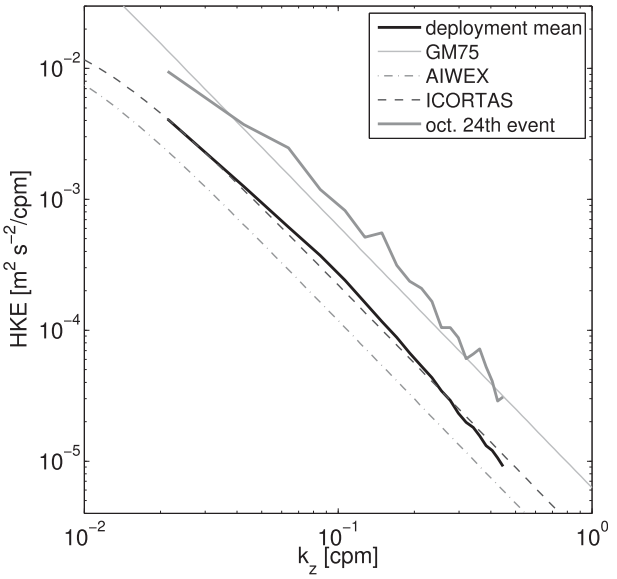

FIG. 6. Mean spectral kinetic energy densities from the moored profiler at mooring I3 from August until the MMP stopped profiling in December 2008 (thick black line). The GM75 spectrum fit to the ICORTAS observations ($j_* = 34$, $E_0 = 3.5 \times 10^{-6}$) is more energetic than AIWEX ($j_* = 20$, $E_0 = 3.6 \times 10^{-6}$) and less energetic than lower-latitude GM75 ($j_* = 6$, $E_0 = 6.3 \times 10^{-5}$) observations. Spectral energies during ICORTAS can be larger than GM75, for example, during a 1.5-day-long wind event starting 24 Oct (thick gray line).

during AIWEX ($E_0 = 3.6 \times 10^{-6}$, $j_* = 20$) (D'Asaro and Morison 1992), but ~10 times smaller than theoretical GM75 values ($E_0 = 6.3 \times 10^{-5}$, $j_* = 6$), similar to observations by Levine et al. (1985) and D'Asaro and Morehead (1991). Spectral energy levels during ICORTAS can be pushed near or above GM75 values during strong near-inertial events, but are still much less than subpolar values even when ice free. Similar spectral energy levels between ICORTAS and AIWEX agree with analysis of recent and historical velocity profiles by Guthrie et al. (2013), which determined there are no significant trends in internal wave energy and mixing in the Arctic. The wavenumber content during AIWEX and ICORTAS are both significantly higher than GM values.

d. Near-inertial band energetics

Baroclinic energy variability in the near-inertial band is a measure of how the strength of the near-inertial internal wavefield changes from ice-free to ice-covered conditions. For internal waves, the ratio of the HKE to the available potential energy (APE),

$$\frac{\mathrm{HKE}}{\mathrm{APE}} = \frac{\omega^2 + f_{\mathrm{local}}^2}{\omega^2 - f_{\mathrm{local}}^2}, \tag{3}$$

is only dependent on the wave frequency ω and the local inertial frequency f_{local}. Horizontal kinetic energy and

available potential energy are HKE = $0.5\rho_0\langle u^2 + v^2\rangle_t$ and APE = $0.5\rho_0 N^2\langle\zeta^2\rangle$, respectively, where u is the zonal velocity, v is the meridional velocity, ρ_0 is the depth-mean density, N is the buoyancy frequency, ζ is the vertical displacement of isopycnals, and $\langle\rangle_t$ is the temporal average over the frequency of interest (Gill 1982). Since inertial frequencies increase moving toward the poles and freely propagating internal waves may only exist between $f^2_{\text{local}} < \omega^2 < N^2$, near-inertial internal waves are constrained to only propagate southward (northward) in the Northern (Southern) Hemisphere to satisfy $f^2_{\text{local}} < \omega^2$. In the Arctic, the near-inertial frequency bandwidth is $f_{\text{local}} \le \omega \le f_{90°}$, as seen in Fig. 4, where the near-inertial peak is mostly constrained between these two frequencies. From Eq. (3) it can be seen that the relatively narrow near-inertial bandwidth will lead to wind-generated internal waves having much larger kinetic energy than potential energy.

The frequency range of the internal wave spectrum also varies as the local effective inertial frequency f_{eff} is modified by background vorticity, where $f_{\text{eff}} \approx f_{\text{local}} + \zeta/2$ and the relative background vorticity is $\zeta = 0.5(\partial U/\partial x - \partial V/\partial y)$ (Kunze 1985), where U and V are low-passed velocities (cutoff = 2 days), changing the width of the internal wave band to $f_{\text{eff}} \le \omega \le N$. Local background vorticity modifies the local inertial frequency from $1.4 \times 10^{-4}\,\text{s}^{-1}$ to effective values of $1.5 \times 10^{-4}\,\text{s}^{-1}$ down to $1.2 \times 10^{-4}\,\text{s}^{-1}$. When above $f^2_{\text{eff}} > \omega^2$, the southward propagation of near-inertial internal waves can be inhibited. When $f^2_{\text{eff}} < f^2_{\text{local}}$, the near-inertial bandwidth increases and the ratio of horizontal kinetic energy to available potential energy decreases [Eq. (3)]. Near-inertial internal waves generated at the North Pole ($\omega = f_{90°}$) and observed at the array can have potential energies that range from 6% to 16% of the total energy. This represents an upper bound on the percentage of the total energy that is potential as the ratio of HKE to APE will increase for waves generated at lower latitudes. Horizontal kinetic energy is therefore a reasonable estimate of the total internal wave energy in the near-inertial band.

Near-inertial HKE in the upper 100 m is elevated when ice is absent, $\overline{\text{HKE}} = 0.58\,\text{J m}^{-3}$ when the percent of ice cover = 0, and reduced when ice is present, $\overline{\text{HKE}} = 0.40\,\text{J m}^{-3}$ when the percent of ice cover is >90 (Fig. 7). However, even during the wintertime, brief periods of enhanced HKE are observed at all moorings. It is also notable that the largest observed value of HKE at moorings, I1, I2, I3, and BS3, is observed during an event in mid-December when the region was mostly ice covered. This December event is examined in more detail in section 3g. By early July, most of the ice has melted and near-inertial HKE rebounds.

Beneath the 100-m surface layer, periods of enhanced HKE ($>0.15\,\text{J m}^{-3}$) are observed down to 600 m (H = 1886 m) during the ice-free and ice-forming period until mid-November when the region becomes ice covered (Fig. 8b). Packets generated at the surface on 20 August, 20 September, 10 October, and 20 October can be traced below 400 m. This suggests near-inertial internal waves generated at the surface can propagate into the Beaufort Sea interior at the mooring site, but this may not hold in other regions of the Arctic where atmospheric forcing, stratification, or ice concentrations are different. After 10 November, when ice concentrations rise above 90%, near-inertial HKE decreases from the surface down to 600 m. Below 300 m, the average depth-integrated HKE decreases ~40% from ice-free values of $9.6\,\text{J m}^{-2}$ to ice-covered values of $5.8\,\text{J m}^{-2}$ (Fig. 8c). Near the surface ($z < 58$ m), mean HKE decreases ~60% from $34.4\,\text{J m}^{-2}$ to $13.5\,\text{J m}^{-2}$ (Fig. 8a).

The moored profiler stopped profiling after 3 December, so it is unclear if near-inertial internal waves generated during the strong mid-December event propagated into the ocean interior. Surface kinetic energies are large during the mid-December event ($>2\,\text{J m}^{-3}$), similar to other surface kinetic energy events with a corresponding deep near-inertial response, suggesting that internal waves could be generated. However, it is unclear whether internal waves generated when sea ice is present can even propagate into the interior, particularly if they are dissipated by sea ice as suggested by Morison et al. (1985).

e. *Upward- and downward-propagating internal wave variability*

Because of their similar frequencies, tidal- and wind-generated internal waves cannot be easily distinguished by frequency at this latitude. To distinguish near-inertial waves from internal tide, it is useful to divide observations in the semidiurnal band into upward- and downward-propagating components.

Internal waves generated by winds initially propagate downward from the sea surface, while those generated by tides initially propagate upward from the seafloor. Upon reaching either the sea floor or surface in an ice-free ocean, internal waves are reflected, causing a change in their vertical direction. Observations of up- and downward shear by Pinkel (2005) suggest that in an ice-covered ocean near-inertial internal waves conform to a "one-bounce" model, where upward-propagating waves that have been either generated or reflected from the bottom are absorbed at the surface in the underice boundary layer. Therefore, underice, downward-propagating, semidiurnal waves are expected to be predominantly wind generated, while upward-propagating waves can be

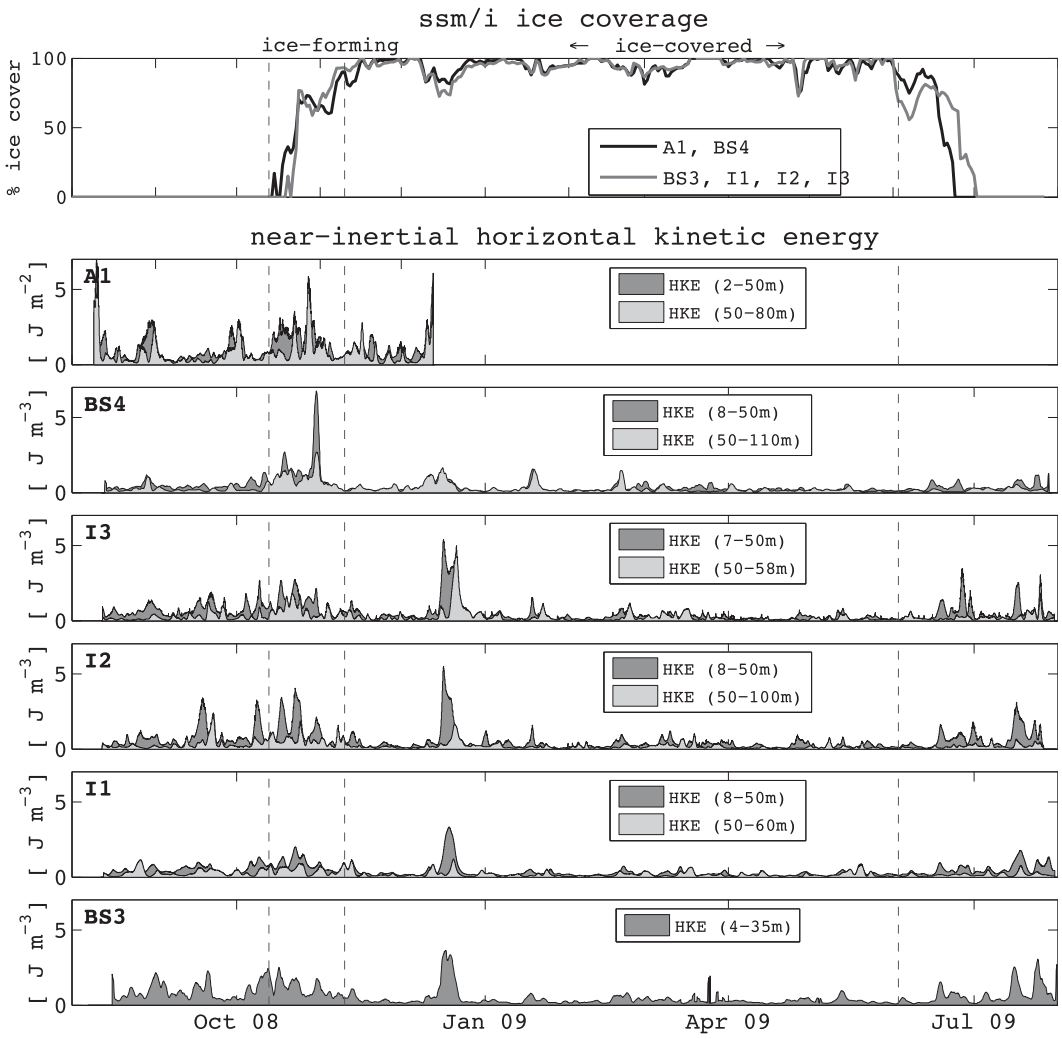

FIG. 7. Depth-averaged horizontal kinetic energy in the near-inertial band above and below 50 m on the Beaufort slope (A1 and BS4) and shelf (BS3, I1, I2, and I3). Depth ranges for each instrument are in the caption. The ADCP at A1 stopped sampling on 13 Dec 2008, and there is no data below 50 m at BS3 (Table 1).

either tidal or wind generated. The direction of vertical propagation is determined by the sense of rotation of velocity and shear with depth (Leaman and Sanford 1975). Downward-propagating (upward) internal waves have velocity and shear vectors that rotate clockwise (anticlockwise) with increasing depth.

Shear S is calculated from the velocity, where shear variance is

$$S^2_{10\mathrm{m}} = \left(\frac{\partial u}{\partial z}\right)^2 + \left(\frac{\partial v}{\partial z}\right)^2, \qquad (4)$$

calculated over 10-m intervals (dz). Shear vectors that rotate clockwise and anticlockwise with depth are separated using spectral methods following Leaman and Sanford (1975). Only at mooring I2 is the vertical range of the ADCP below the mixed layer large enough (50–100 m corresponding to 13 4-m bins) to separate the vertical shear profiles into upward- and downward-propagating components. To exclude possible biasing by ice–ocean boundary layer shear, only near-inertial shear below 50 m is examined.

From the ADCP data at I2, downward shear variance from 54 to 94 m is larger than upward shear variance, suggesting the bulk of internal waves are downward propagating, most likely generated by winds (Fig. 9). Downward shear is episodically large throughout the year. Bursts of increased downward shear variance lasting 3–7 days are observed during ice-covered conditions, suggesting near-inertial internal waves are generated by

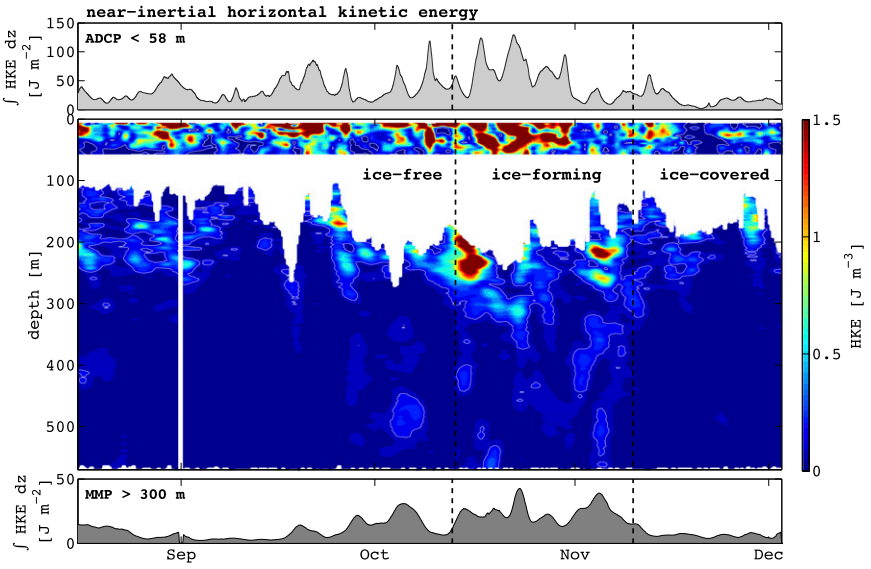

FIG. 8. (top) Near-inertial HKE depth integrated from 0 to 58 m from the ADCP at mooring I3. (middle) Depth–time series of near-inertial HKE from MMP data. Average HKE as measured by the MMP is 0.1 J m^{-3} and denoted by the white contour. (bottom) Depth-integrated near-inertial HKE kinetic energy from 300 to 550 m.

winds even when the ocean is ice covered. Downward shear variance is largest during the ice-forming period and, surprisingly, slightly larger when ice covered than when ice free (Table 3). Ice-free shears are quasi-continuously elevated to $\sim 0.2 \times 10^5\,\mathrm{s}^{-2}$, while ice-covered shears are generally smaller $\sim 0.1 \times 10^5\,\mathrm{s}^{-2}$, but punctuated by strong events in December and March ($>1 \times 10^5\,\mathrm{s}^{-2}$). Internal wave shear is clearly event driven throughout the year, and it is unclear from only 1 yr of data whether the seasonal averages are representative of the Beaufort Sea internal wave climatology. However, monthly means illustrate shear decreases over the course of the winter from a high value of $0.37 \times 10^5\,\mathrm{s}^{-2}$ in December to a low value of $0.08 \times 10^5\,\mathrm{s}^{-2}$ in April and is generally low, $<0.25 \times 10^5\,\mathrm{s}^{-2}$, during the ice-free summer, similar to the seasonal pattern of monthly-mean wind stress. Strong individual shear events, particularly during December and March, may obscure what is likely a weak annual cycle of shear that is similar to the seasonal cycle of kinetic energy in the mixed layer.

f. *Flux from winds to inertial oscillations*

Periods of strong wind stress, lasting 3–4 days, occur throughout the year when the Beaufort is both ice covered and ice free (Fig. 10). Typically, a large oceanic response is expected when the wind stress is large. This is true during the ice-free season when increased wind stress corresponds with increased near-inertial kinetic energy in the mixed layer. However, during the winter mixed layer, near-inertial kinetic energy is significantly reduced while wind stresses remain high (the notable exception is the December event discussed in section 3g), suggesting sea ice modifies the surface response to wind stress. In the following sections, it will be shown that a strong and consolidated ice pack damps near-inertial motions in the mixed layer and inhibits energy flux from

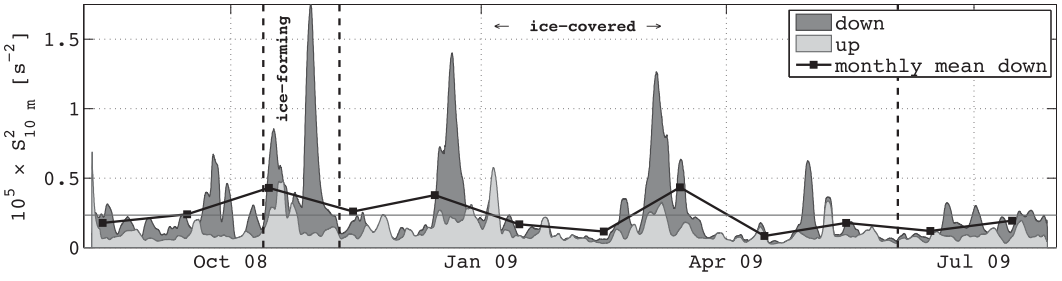

FIG. 9. Depth-integrated upward and downward near-inertial shear variance at mooring I2 below the bottom of the mixed layer (50–100 m) smoothed with a 3-day sliding boxcar. Monthly-mean clockwise near-inertial shear variance is denoted by the thick black line and the annual mean by the horizontal thin gray line.

TABLE 3. Depth-mean up- and downward semidiurnal shear below the mixed layer (50–100 m) during ice-free, ice-forming, and ice-covered periods. Standard errors for all values are $<0.01\ \mathrm{m^2\,s^{-2}}$.

$10^5 \times S^2_{10\mathrm{m}}\ (\mathrm{s^{-2}})$	Ice free	Ice forming	Ice covered
Up	0.09	0.20	0.12
Down	0.19	0.57	0.21

the atmosphere to the mixed layer, reducing the potential for near-inertial internal wave generation.

The mechanisms by which internal waves are generated by winds when ice is present or absent are similar. When the ocean is ice free, the mixed layer responds by oscillating at the local inertial frequency. Local variations in wind stress cause the divergence and convergence of horizontal currents, pumping the mixed layer to create internal waves that radiate downward into the ocean interior. When the ocean is ice covered, the ice and the mixed layer oscillate together as a slab at the local inertial frequency, coupled by ice–ocean drag, and generate internal waves through the same process as when ice free.

To examine the modification of the ocean response to wind stress, a slab model (Pollard and Millard 1970) is employed. The slab model predicts the surface mixed layer inertial response using wind stress and is used because the mixed layer inertial oscillations are driven by wind stresses resonant at the local inertial frequency rather than increased wind stress magnitude. Of course stronger wind stresses will produce a larger inertial response, but only if they are resonant.

The slab model is applied during both ice-free and ice-covered conditions, but it can only model the upper-ocean response in an ice-free ocean. While this assumption is limited, it does allow the exploration of the potential for storms to excite a near-inertial response. In particular, slab model results (which is the expected ice-free response) and observations (where the response is modified by sea ice) are compared in order to determine the effect of ice–ocean stress based on differences between the two. The effect of ice–ocean stress has been examined in an ice–ocean model developed by McPhee (1978), which predicts the inertial response of ice and ocean to resonant atmospheric forcing, but also incorporates surface sea ice drag. While the McPhee (1978) model may better describe the vertical profile of horizontal velocity in the upper-water column than the (Pollard and Millard 1970) slab model, the slab model is used to quantify the change in the ocean response to sea ice cover and whether decreased wintertime near-inertial kinetic energy is due to sea ice damping or merely unfavorable winds.

Following Pollard and Millard (1970) and D'Asaro (1985), the inertial currents in the mixed layer are modeled by

$$\frac{du_{\mathrm{ml}}}{dt} - fv_{\mathrm{ml}} = \frac{\tau_x}{H\rho} - ru_{\mathrm{ml}}, \quad \text{and} \tag{5}$$

$$\frac{dv_{\mathrm{ml}}}{dt} + fu_{\mathrm{ml}} = \frac{\tau_y}{H\rho} - rv_{\mathrm{ml}}, \tag{6}$$

where u_{ml} and v_{ml} are the mixed layer horizontal velocities, τ_x and τ_y are the zonal and meridional wind stresses, H is the mixed layer depth, ρ is the density, and r is a decay constant. The solution to the equations above produce mixed layer velocities that are the sum of Ekman and inertial velocities, $u_{\mathrm{ml}} = u_E + u_I$. Inertial velocities in the mixed layer are only forced by changes in wind stress (compared to Ekman velocities that are forced by constant wind stress) and solved for following D'Asaro (1985). The decay constant is set to $r = 0.15f$, which corresponds to a ~3.5-day decay scale following Alford (2001). There are no other similar studies in the Arctic that the authors are aware of, and this is similar to the ice-free 3-day decay scale estimated in section 3h. The decay constant is likely modified by ice mechanics when ice is present, but changes in its value are not accounted for here.

The predicted energy transferred from the wind to near-inertial motions is

$$\Pi = \tau \cdot \mathbf{u}_I, \tag{7}$$

where Π is the power per unit area or the energy flux across the ocean surface, and $\mathbf{u}_I$ represents the inertial currents predicted by Eqs. (5) and (6). Power is positive when wind stress and the inertial currents are in the same direction and indicates energy transfer from the atmosphere to the mixed layer. Energy is most efficiently transferred from the atmosphere to the ocean when the winds are resonant with inertial currents in the mixed layer, causing inertial currents to increase. By comparing the predicted flux to the observed mixed layer near-inertial kinetic energy, the modification of the mixed layer response to sea ice and the potential for near-inertial internal wave generation can be examined.

The slab model is sensitive to changes in the mixed layer depth. Predicted currents increase when the mixed layer is shallow and decrease when it deepens. Similarly, Π increases when mixed layer depths decrease. To account for the sensitivity, mixed layer depths from the Arctic winch are input to the slab model rather than a constant mixed layer depth. Although there are unaccounted spatial gradients in mixed layer depths, the differences are expected to be smaller than 10 m as mean

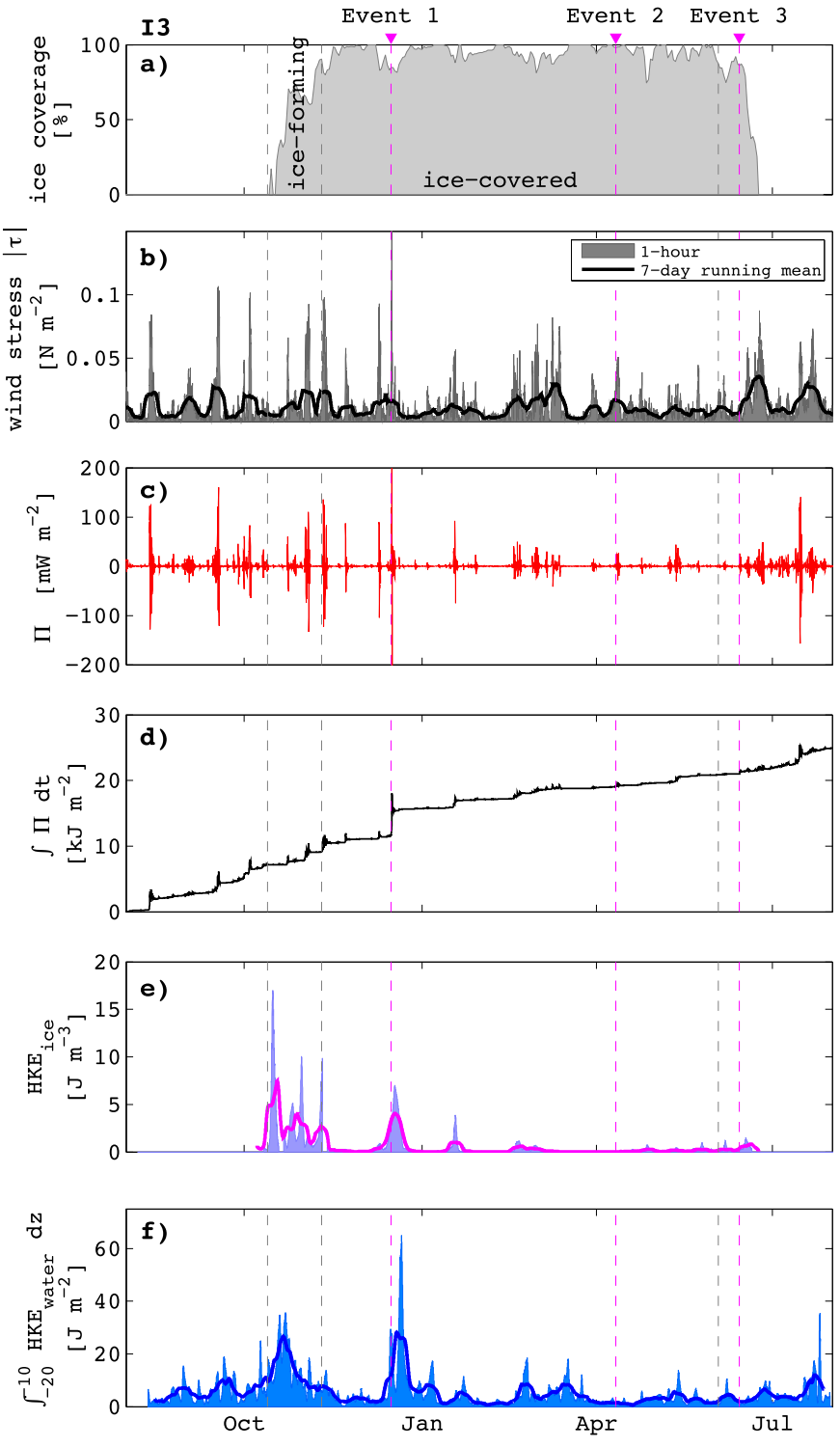

FIG. 10. (a) Ice coverage from SSM/I, (b) wind stress from Prudhoe Bay, (c) energy flux from wind to near-inertial motion, (d) net energy transfer, (e) near-inertial horizontal kinetic energy of ice, and (f) depth-integrated near-inertial horizontal kinetic energy from 10 to 20 m (which is nearly always in the mixed layer). Boundaries of the ice-forming and ice-covered periods are the vertical gray lines, and the timing of the events discussed in section 3g are indicated by the vertical magenta lines.

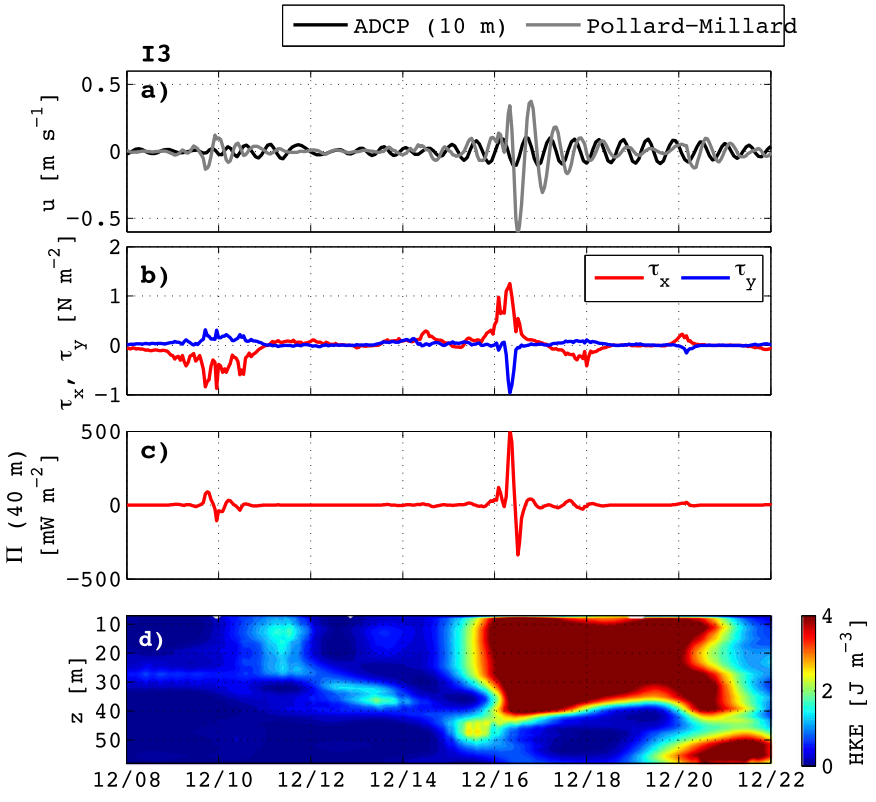

FIG. 11. (a) Comparison of observed near-inertial zonal velocities at I3 (black) during the 2-week period after 8 Dec 2008 to those predicted by the Pollard–Millard mixed layer slab model (gray), (b) wind stress used to force the model, (c) prediction of energy flux from the winds to near-inertial motion in the mixed layer, and (d) near-inertial kinetic energy in the upper 60 m.

winter and summer depths on the slope are similar to those in the central Canada basin (Toole et al. 2010). The standard error for Π is 26.6 m W m^{-2} when using a constant mixed layer depth that deviates up to 40 m from observations, while it is only 4.4 m W m^{-2} when an error of ±10 m is assumed for the Arctic winch data and smaller than the annual standard error of Π, which is 15 m W m^{-2}.

When compared with observations, the slab model reproduces mixed layer kinematics well during some wind events but not others. The predictions are still useful to estimate the potential wind energy available for internal wave generation. An event that shows good agreement occurred on 16 December 2008 (Fig. 11). The mixed layer depth during this time is 18.75 m, and it can be seen that both the near-inertial velocity (Fig. 11a) and kinetic energy (Fig. 11d) in the mixed layer increase in response to a change in wind stress (Fig. 11b) and increased flux (Fig. 11c). Inertial velocities in the mixed layer predicted by the Pollard–Millard model are in phase but somewhat larger than observations that may be damped by ice stress. While not the case during this event, the predicted velocities can be out of phase with the observed velocities, lagging or leading the observations by up to 6 h. This can be attributed to the physical separation between the wind data collected at Prudhoe Bay and the moored array (~150 km), which may be affected by regional differences in mesoscale atmospheric circulation. Following the event, there is a burst of near-inertial kinetic energy below the mixed layer on 20 December with near-inertial velocities having upward-phase propagation (not shown), suggesting this event generated downward-propagating near-inertial internal waves.

Although the velocities are not always well predicted, the slab model does typically predict increased kinetic energy in the mixed layer when there is an increase in Π, the energy flux from the atmosphere to near-inertial motions. The slab model flux Π is more strongly correlated, albeit weakly, to mixed layer near-inertial kinetic energy ($\rho = 0.16, p < 0.01$) than either wind stress or slab model–predicted mixed layer kinetic energy because it takes into account whether the forcing is resonant at the local inertial frequency. Weak correlations are expected since the wind data used to force the model is from a remote source, the mixed layer response is modified by ice, and inertial oscillations in the mixed layer can also

be caused by low-mode near-inertial internal waves. Nonetheless, the flux calculated using the slab model can be a reasonable predictor of the expected oceanic inertial response to atmospheric forcing.

Flux from the atmosphere to near-inertial motions is episodic (Fig. 10). When increased flux to inertial motions is predicted, near-inertial ice and ocean kinetic energies also increase. Usually, flux is smaller than 10 m W m^{-2}, but large isolated events are predicted throughout the year. The largest event occurs in mid-December (>200 m W m^{-2}) and coincides with large inertial responses in both the ice and the ocean. Smaller events (40–100 m W m^{-2}) occur when the ocean is both ice free and ice covered.

While flux events occur throughout the entire year, the duration of the oceanic response is modulated by the presence of ice. When the region is ice free from July to mid-October, increased HKE_{water} occurs when there are peaks in flux from the wind to inertial oscillations in the mixed layer, remaining elevated for several days afterward. When the region is ice covered from mid-November to July, both HKE_{water} and HKE_{ice} increase in phase with the wind flux, but quickly decrease within 1–2 days (or 3–4 inertial periods after the event). Unlike the ice-covered period, near-inertial HKE_{ice} and HKE_{water} does not quickly decay after flux events during the ice-forming period from mid-October to mid-November, and HKE_{water} is similar to ice-free values. This suggests the structure of the ice pack during the ice-forming period may allow near-inertial oscillations to persist. During the ice-forming period, SSM/I ice concentrations are low, which indicates a weak and fragmented ice pack that may be more easily stirred by winds and allow near-inertial oscillations to persist. However, SSM/I data are known to be biased and may underpredict ice coverage by 5%–10% during the ice-forming period (Partington and Bertoia 1999). Increased kinetic energy in the absence of a flux event also occurs during the ice-free and ice-forming periods (for example in September 2008) and is likely caused by the passage of near-inertial waves that were generated elsewhere past the array.

Underice roughness could potentially lead to faster decay times due to increased ice–ocean stress. However, the effects of underice roughness cannot be quantified as the ADCP's are unable to resolve surface roughness at wavelengths less than 50 m, and to the author's knowledge there is not any literature on the seasonal variability of underice roughness in the Arctic. Any discussion of roughness on the decay scale is purely speculative. Ice surface roughness is related to ice age, increasing through deformation and reducing for old ice through summer melt, but how ice roughness changes throughout the deployment is unknown, and seasonal variability may be small when compared to the effects of ice age and sporadic deformations. From the observations it is determined that increased underice roughness is an unlikely cause of decreased decay times. When excited by resonant winds, the ice and ocean are always strongly coupled, moving together at the inertial frequency (Fig. 10). Even as the inertial amplitude decays, the ice and ocean continue to move together. If ice–ocean drag caused near-inertial current decay, we would expect the ice and mixed layer to become decoupled as the inertial oscillations decay, which they do not. This suggests that inertial oscillation decay time scales are dependent on ice mobility and thickness rather than underice roughness.

These observations suggest both the ocean and the ice respond to resonant atmospheric forcing throughout the year, but the rapid decline in kinetic energy after periods of elevated flux from winds to the mixed layer from November to June suggest a consolidated and strong ice pack heavily damps near-inertial motions. These observations are similar to those by McPhee (1978), who also observed increased damping of surface inertial velocities in midwinter. By examining all observed near-inertial events, damping time scales between ice-free and ice-covered periods are quantified and compared in section 3h.

g. *Case studies*

To determine the effect of ice concentration and strength on near-inertial motions due to atmospheric forcing, three different events during the 2008/09 winter are examined when ice is detected over the moorings. Ice divergence [Eq. (1)], ice maximum shear strain rate [Eq. (2)], and ice concentration are compared to the predicted flux from winds to mixed layer near-inertial oscillations and observed near-inertial kinetic energies in the mixed layer to determine that conditions allow for the transfer of energy from the atmosphere to the ocean via sea ice.

1) EVENT 1: 16 DECEMBER 2008

The largest flux event occurs during an event on 16 December 2008. It is preceded by a smaller event on 10 December. The earlier event may allow more energy transfer from the atmosphere to the ocean during the later 16 December event by preconditioning the ice and is also discussed to provide context for the observed ice–ocean response to resonant forcing.

The 16 December event occurs in midwinter when ice concentrations are high (>80) (Fig. 10, vertical magenta line). In addition, the largest annual near-inertial kinetic energies observed during the deployment occur in the upper 30 m and remain elevated for nearly 5 days. The mixed layer depth is 18.75 m, shallower than the ice-covered mean of 22 m and along with strong resonant

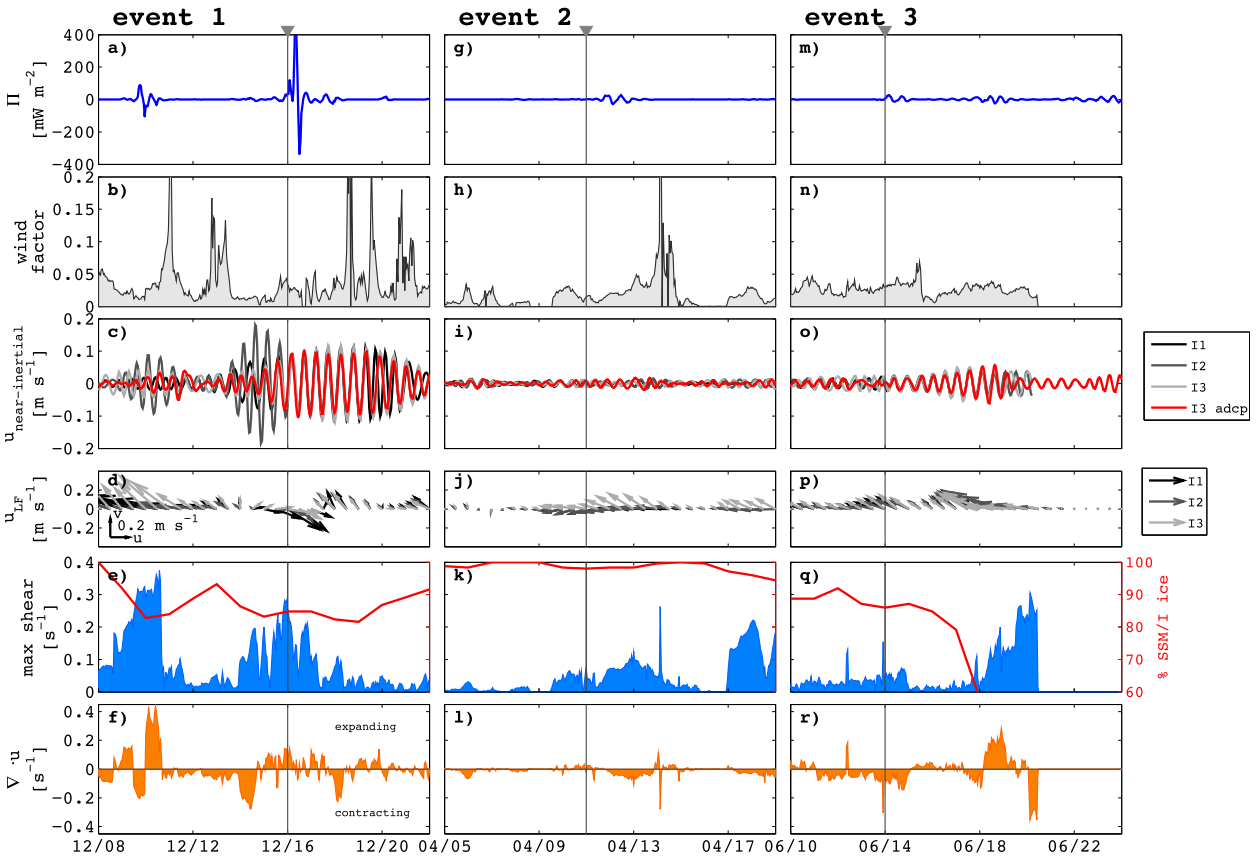

FIG. 12. (a)–(f) Event 1 (16 Dec 2008), (g)–(l) event 2 (11 Apr 2009), and (m)–(r) event 3 (14 Jun 2009) as discussed in section 3g. (top to the bottom) Power from wind to near-inertial oscillations, wind factor ($|u_{ice}|/|u_{wind}|$), near-inertial ice (gray) and water velocity (red), low-frequency ice drift (gray arrows), maximum shear strain rate of ice (blue) and SSM/I ice coverage (red), and ice divergence ($\mathbf{V} \cdot \mathbf{u}$).

winds is responsible for the large fluxes from winds to near-inertial motions in the mixed layer. Three days after the event near-inertial HKE and downward shear below the mixed layer (>30 m) are more than 10 times the preevent values, suggesting internal waves are generated and near-inertial energy is propagating downward beneath the mixed layer (not shown).

Satellite ice concentrations decrease to nearly 80% during the week before and after the event, suggesting a change in ice pack strength may allow the large inertial response to persist for 5 days (Figs. 12a–f). Starting 3 days prior to the event, ice shear strain rates increase and ice divergence fluctuates indicating a weaker ice pack. Low-frequency ice velocities are elevated and the wind factor also increases showing a strong ice response to increased wind forcing and suggests ice movement is not inhibited by interactions with ice or land-fast ice on the continental shelf. In addition, near-inertial velocities in the ice and mixed layer are in phase and of similar magnitude, indicating the ice pack and mixed layer move together in coherent inertial circles over moorings I1–I3. This is expected as the mixed layer is within the range of the frictional influence of ice (~35 m) (McPhee 1978). At all moorings, but particularly at I2, near-inertial velocities start to increase about 1.5 days before the event and may be due to the propagation of near-inertial waves through the array that were generated upstream by the same storm.

Preceding the 16 December event, there is another resonant wind event on 10 December. During this earlier event, both the flux from winds to mixed layer near-inertial oscillations and the near-inertial response are smaller. Inertial oscillations also die out faster, within two inertial periods. For 2 days preceding and during the 10 December event, ice shear strain rates are even larger than during the 16 December event, but drop immediately afterward, suggesting a decrease in ice mobility. Inertial motions may persist after the 16 December event due to the ice pack possibly being preconditioned by the earlier event, which "loosens" the ice and weakens ice–ice interactions and suggests closely spaced flux events may allow more energy input in the near-inertial band.

The moored profiler stopped profiling after 3 December, so it is unclear if near-inertial internal waves

generated during the 16 December event propagate below 100 m. Surface kinetic energies ($>200\,\mathrm{J\,m^{-2}}$) and shears ($>1 \times 10^{-5}\,\mathrm{s^{-2}}$) are large, similar to other events during September and October with a corresponding, deep, near-inertial response, suggesting that internal waves are likely generated.

2) EVENT 2: 11 APRIL 2009

A weaker flux event is predicted during the ice-covered season on 11 April 2009 (Fig. 12, middle column). Near-inertial ice velocities are weak, incoherent across the array, and are out of phase with near-inertial mixed layer velocities. The slab model predicts a large flux from winds to mixed layer near-inertial oscillations and the mixed layer depth (21.45 m) is similar to the ice-covered average, but the weak, near-inertial response suggests atmospheric energy is not transferred to near-inertial oscillations in the mixed layer. The wind factor is not particularly low before the event, and low-frequency ice velocities increase somewhat before the event, indicating the wind should be able to move the ice pack. There is a slight increase in near-inertial shear below the mixed layer, doubling from preevent values, but is still at 75% below the annual mean, suggesting the event may have generated very weak internal waves, if any at all.

Even though ice concentrations are near 100%, ice shear strain rates increase, suggesting the ice pack is still somewhat fragmented and mobile, but much less so than during the December event. Earlier events with similar flux magnitudes during the ice-forming period (not shown), when ice concentrations decrease and ice shear strain rates increase, excite larger near-inertial oscillations in the mixed layer that are in phase across the array. This suggests that increased ice concentrations and a decrease in ice mobility inhibit near-inertial oscillations.

3) EVENT 3: 14 JUNE 2009

A third event occurs on 14 June 2009 when ice coverage is above 80% and is followed by another event on 18 June 2009, when ice concentrations have decreased to below 60% (Fig. 12, right column). By comparing these two closely spaced events of similar flux magnitude during the annual ice retreat, it can be seen how reductions in ice pack strength potentially allow near-inertial internal wave generation under ice.

During the 14 and 18 June events, fluxes from winds to mixed layer near-inertial oscillations and wind factors are similar, while ice concentration, ice shear strain rates, and ice divergence are not. Inertial oscillations are excited during the 14 June event, but are weak and incoherent across the array. In contrast, inertial oscillations excited in both the ice and mixed layer during the 18 June event are large and in phase. Before the 14 June event, downward near-inertial shear below the mixed layer remains constant, but increases by nearly 500% after the 16 June event. During both events the depth of the mixed layer is below 31 m. The differences in the near-inertial response suggest that decreased ice mobility, indicated by decreased ice shear strain rates and ice divergence magnitude, inhibits energy transfer from the atmosphere to near-inertial motions and the generation of internal waves. This is consistent with observations during event 2 in April, when a flux event of similar magnitude did not produce significant near-inertial oscillations.

h. Damping time scales

In the previous section, the near-inertial response to resonant winds is shown to be dependent on ice pack strength. High ice concentrations and decreased ice mobility during the winter inhibits near-inertial oscillations in the ice–ocean boundary layer and therefore internal wave generation as well. In an ice-free ocean, the response to atmospheric forcing is typically characterized by a sudden increase in near-inertial kinetic energy that then decays over several days. As noted in section 3f, near-inertial kinetic energies appear to decay more rapidly when the moorings are ice covered (Fig. 10). Using the observations, near-inertial decay scales during ice-free and ice-covered periods are calculated and compared to determine the attenuation of near-inertial oscillations by sea ice.

Previous studies have determined decay scales by fitting mixed layer velocity predictions from the slab model to observations (Alford 2001). Decay scales could not be determined using this method as the wind data are from Prudhoe Bay over 150 km away, and the predictions tended to lag or lead the observations by 0–6 h, depending on the wind direction. Instead, the magnitude and decay of the oceanic response to wind forcing is determined by examining the spindown of near-inertial kinetic energies in the mixed layer after a flux event.

Near-inertial energy in the mixed layer is estimated by depth-averaging kinetic energies from 10–20 m at moorings I1–I3. This is well within even the shallowest mixed layer depth and within the ice–ocean frictional boundary layer, but far enough from the surface to ensure there are no data gaps due to mooring blowdown. The decay of near-inertial velocity following the initial input of energy is assumed to be logarithmic. Thus, fitting a decaying exponential to each flux event solves for both the decay scale and its inverse, the decay constant r. The fit is sensitive to window length and fits are made over a range of windows (from 0.5 to a 5-day maximum to minimize overlap between successive wind events), taking the average value as the decay scale. The fit is

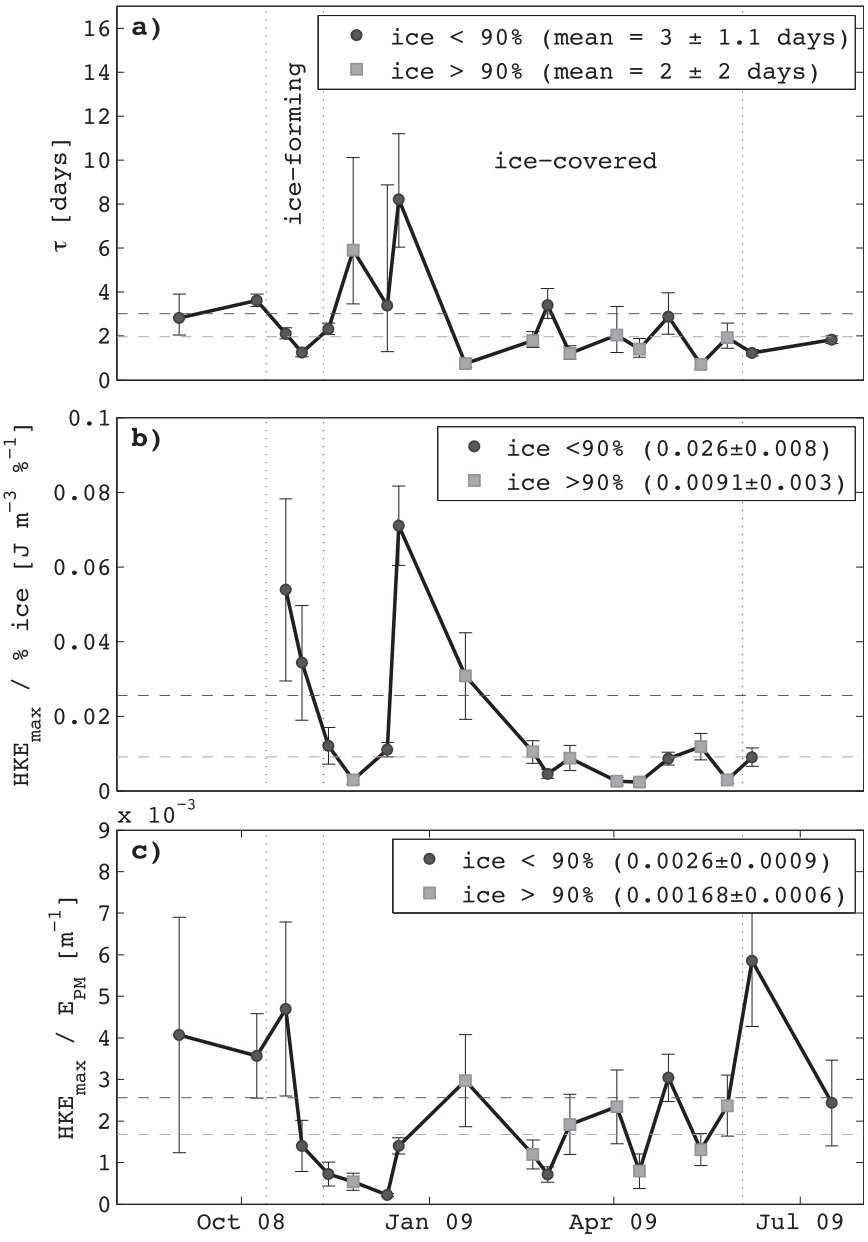

FIG. 13. (a) Mean exponential decay scales during resonant events when near-inertial HKE events in the mixed layer increase and there is a potential for internal wave generation. Whiskers indicate one standard deviation of estimates. (b) Ratio of maximum observed horizontal kinetic energy to ice concentration during the events. (c) Ratio of maximum observed horizontal kinetic energy to energy transferred from the atmosphere to inertial motions from the slab model. In all panels, local ice concentrations $< 90\%$ are black circles and $> 90\%$ are gray squares. Mean values and standard errors are listed in the legend and plotted as black and gray horizontal lines.

constrained to pass through the maximum kinetic energy within 2 days after the start of the event.

Decay scales range from 0.9 to 4 days (Fig. 13a). Even though only a handful of events can be examined during each ice season, it is still possible to get sense of the effect of sea ice on the damping time scales and compare these results to midlatitude values by examining the decay constant that is adjusted for f_{local}. When ice concentrations are reduced below 90%, the mean decay scale is 3.0 ± 1.1 days, corresponding to $r = 0.18(0.13 - 0.28)f_{\text{local}}$. The ice-free decay constant is indistinguishable from values calculated at lower latitudes where there is no

seasonal ice ($r = 0.15f_{34°N}$; Alford 2001). When ice concentrations are elevated above 90%, the mean decay scale is shorter, 2.0 ± 2.0 days, corresponding to $r = 0.26(0.13 - \infty)f_{local}$. During three events in December, decay scales (>4 days) are significantly longer than the mean values, biasing their values (2.4 ± 1.1 days for ice < 90% and 1.4 ± 1.6 days for ice > 90% when removed) but still resulting in longer decay scales when ice concentrations decrease. While the mean decay scales are statistically indistinguishable and more results are needed to make a definite conclusion, the results suggest that decay times shorten when ice concentration is high.

Decreased decay times suggest that once excited, near-inertial motions in the mixed layer are more quickly damped when ice concentrations are above 90%, conditions that are typical after December. During this period the ice pack can be immobile for 1–2 weeks or longer as the ice grows and multiyear ice drifts near the moorings. This stronger ice pack inhibits near-inertial oscillations. First-year ice is predominant from November to December when ice concentrations range from 60% to 90% and coincide with shorter decay scales. The differences in decay scales between the early winter when the ice pack is thinner and more mobile to late winter when the ice pack is thicker and less mobile reconfirms that ice pack morphology determines the damping time scales of near-inertial oscillations in the mixed layer.

The magnitude of the oceanic response to resonant forcing during wind events is also impacted by the local sea ice concentration (Fig. 13b). When ice concentrations are below 90%, the ratio of the maximum HKE during each event to sea ice concentration increase to $2.6 \pm 0.8 \times 10^{-2}$. When ice concentrations are above 90%, the ratio decreases to $9 \pm 3 \times 10^{-3}$, indicating the magnitude of the inertial response in the mixed layer is sensitive to changes in sea ice concentration.

To determine whether reduced initial HKE magnitude is due to damping by ice or reduced atmospheric forcing, the ratio of the maximum HKE to the energy transferred from the atmosphere is examined using the slab model ($E_{PM} = \int \Pi \, dt$, integrated over 6 days, the event length, where E_{PM} is the flux estimated by the Pollard–Millard slab model). The ratio describes the magnitude of the mixed layer inertial response to atmospheric forcing (Fig. 13c) and varies substantially between events. Mean values decrease from $2.8 \pm 0.9 \times 10^{-3}$, when ice concentrations are below 90%, to $1.7 \pm 0.6 \times 10^{-2}$, when ice concentrations are above 90%, suggesting ice suppresses the initial transfer of energy from the atmosphere to surface inertial motions. Mean E_{PM} is also below average when ice concentrations are below 90% (not shown), suggesting that in addition to decreased energy transfer, typically less atmospheric energy is available for near-inertial wave generation during the winter.

A decrease in efficiency also holds true for exceptionally strong winter storms, such as the December event. On 10 and 16 December, ice coverage decreases to below 80%, and decay scales are longer, 8.6 days, even longer than ice-free periods. However, the ratio of KE_{max} to E_{PM} is small, indicating that when scaled against the other flux events, the near-inertial response is relatively weak, suggesting it is not affected by slight decreases in ice concentration. Rather, it was exceptional wind forcing that caused the large inertial response.

i. Comparison to previous studies

To put these results into context with what is already known about the Arctic internal wavefield, we will compare them with previous observations. Vertical wavenumber spectra from the AIWEX and ICORTAS surveys presented in section 3c have similar energy levels and wavenumber content when compared to GM spectra at lower latitudes. The absence of large changes between AIWEX and ICORTAS might be an indication that the bulk internal wavefield may not have significantly evolved with the loss of sea ice in the Beaufort Sea, although comparisons between ICORTAS and AIWEX surveys are insufficient to make any definitive conclusions. However, a lack of change in the internal wavefield is supported by similar results by Guthrie et al. (2013) that used historical velocity data from expendable current profilers (XCP) current profiles (including AIWEX data) to determine there are no significant trends in internal wave energy and mixing in the Arctic. Variations in topography (Pinkel 2005), forcing (Padman et al. 1992), mixed layer depth, stratification (Guthrie et al. 2013), and ice concentration (Rainville and Woodgate 2009; Dosser et al. 2014) are likely to have greater impacts on internal wavefield strength.

Changes in local bathymetry may account for the minor differences between ICORTAS and AIWEX energy levels and vertical wavenumbers. ICORTAS was conducted over the rough and corrugated Beaufort continental slope, while AIWEX was conducted over the smooth and deep Canada basin. When compared to the abyssal plains, fits to the GM75 model reveal a relatively energetic Arctic internal wavefield over the rough and shallow Yermak Plateau (D'Asaro and Morison 1992; Fer et al. 2010). Similarly, observations from an ice camp that drifted from the deep Canada over the shallow Chukchi Cap showed vertical wavenumber spectra are sensitive to changes in bathymetry (Pinkel 2005).

A seasonal cycle of near-inertial internal wave energy is observed in both the Beaufort and Chukchi Seas, but have significant differences that are likely due to local

changes in forcing. On the Beaufort slope, the largest shear is observed during the ice-forming period from October to November (Table 3), coincident with the enhanced wind stress during the storm season. In the Chukchi, shear is largest from July to August (Rainville and Woodgate 2009), 3 months before the local wind stress peak. The difference in the timing of the shear peak might be due to regional differences in mixed layer depth. In the Chukchi, near-inertial shear decreases from July to November as the base of the surface shear layer increases from 10 to 30 m. In contrast, Beaufort near-inertial kinetic energy remains relatively constant until the autumn storm season, with a relatively constant mixed layer depth of 10 m, only briefly deepening to 15–30 m for 2–5 days after strong wind events. Mixed layer depth is likely an important control of internal wave generation, with gradual and persistent deepening inhibiting internal wave generation later in the Chukchi ice-free season. The annual evolution of the mixed layer depth is variable across the shallow Arctic shelves and therefore large regional differences in internal wave generation should be expected.

There is also a distinct lack of near-inertial shear under ice in the shallow Chukchi (Rainville and Woodgate 2009), but episodic increases in wintertime near-inertial shear have been observed on the continental slope and in the deep Beaufort (Halle and Pinkel 2003). This is surprising, as sea ice in the Chukchi is nearly all first-year ice, which is weaker, likely more mobile, and should be more receptive to resonant wind forcing. The differences between the wintertime near-inertial internal wavefields in the Beaufort and the Chukchi suggest the distribution of wind-generated internal waves is not uniform throughout the Arctic. Their generation may therefore be localized, constrained to regions with favorable conditions.

While the ICORTAS and Chukchi (Rainville and Woodgate 2009) observations indicate the near-inertial internal wavefield has a seasonal cycle that is sensitive to ice cover, in a pan-Arctic study of XCP data, Guthrie et al. (2013) did not attribute variations in bulk internal wave energy to the strength and concentration of the ice pack as a change between winter and spring values was not seen. This is surprising as Dosser et al. (2014) also observed a distinct increase in near-inertial band vertical displacement amplitudes in the central Beaufort when ice concentrations decreased to below 50%. The Guthrie et al. (2013) estimates contain contributions from internal tides and internal wave generation by sea ice (McPhee and Kantha 1989) that could mask a weak seasonal cycle in the near-inertial band, possibly accounting for the differences between the studies.

4. Conclusions

The generation of internal waves is modified by sea ice on the Beaufort continental slope. Near-inertial kinetic energy and shear are largest during the ice-forming season when the ice pack is fragmented and mobile, weakening when it is ice covered and the ice pack is stronger and more consolidated. Spectral energy densities are similar to previous observations in the Beaufort, but are still significantly smaller than at lower latitudes. Kinetic energy packets are observed radiating downward from the surface to 500 m during the summer, suggesting that near-inertial waves propagate deeper than the 500-m Arctic Ocean when ice is not present, but it is still not known how deep near-inertial internal waves can penetrate during the ice-covered season. During the winter, resonant wind stresses excite inertial oscillations in the mixed layer. As sea ice concentrations increase and the ice pack becomes stronger throughout winter, mixed layer oscillations become smaller and are more quickly damped. In addition, when ice concentrations rise above 90%, the atmospheric energy available for internal wave generation is reduced, and energy is less efficiently transferred from the atmosphere to the ocean. While strong wind events may generate internal waves when the sea is ice covered, increased damping and decreased energy transfer are the likely cause of the weak near-inertial internal wavefield in the Arctic.

Of particular concern is the recent reduction of sea ice in the Arctic Ocean and the lengthening of the ice-free season (Stroeve et al. 2012). The rapid loss and diminishing extent of multiyear ice and increase in younger ice suggest a thinner, weaker ice pack (Comiso et al. 2008). The persistence of near-inertial oscillations in the Beaufort Sea during freeze up and melt suggests that an increase in weaker, younger ice may cause a widespread increase in near-inertial energy. Large-scale changes in ice concentrations and strength may lead to longer decay times and longer ice-free seasons, conditions that are favorable for increased near-inertial internal wave generation and internal wave–induced mixing in the Arctic.

Acknowledgments. Kim Martini and Chase Stoudt were supported by NSF Award ARC-0909432. Harper Simmons and Jennifer Hutchings were supported by ONR Award N00014-06-1-0728. Thanks to R. Pickart (Woods Hole Oceanographic Institution) for providing the Arctic winch data used to calculate mixed layer depths for the slab model and ADCP from moorings BS3 and BS4. S. Okkonen (University of Alaska) provided ADCP data for mooring A4. We thank Matthew Alford for his comments on the experimental design and for his assistance in deploying the moorings. The authors

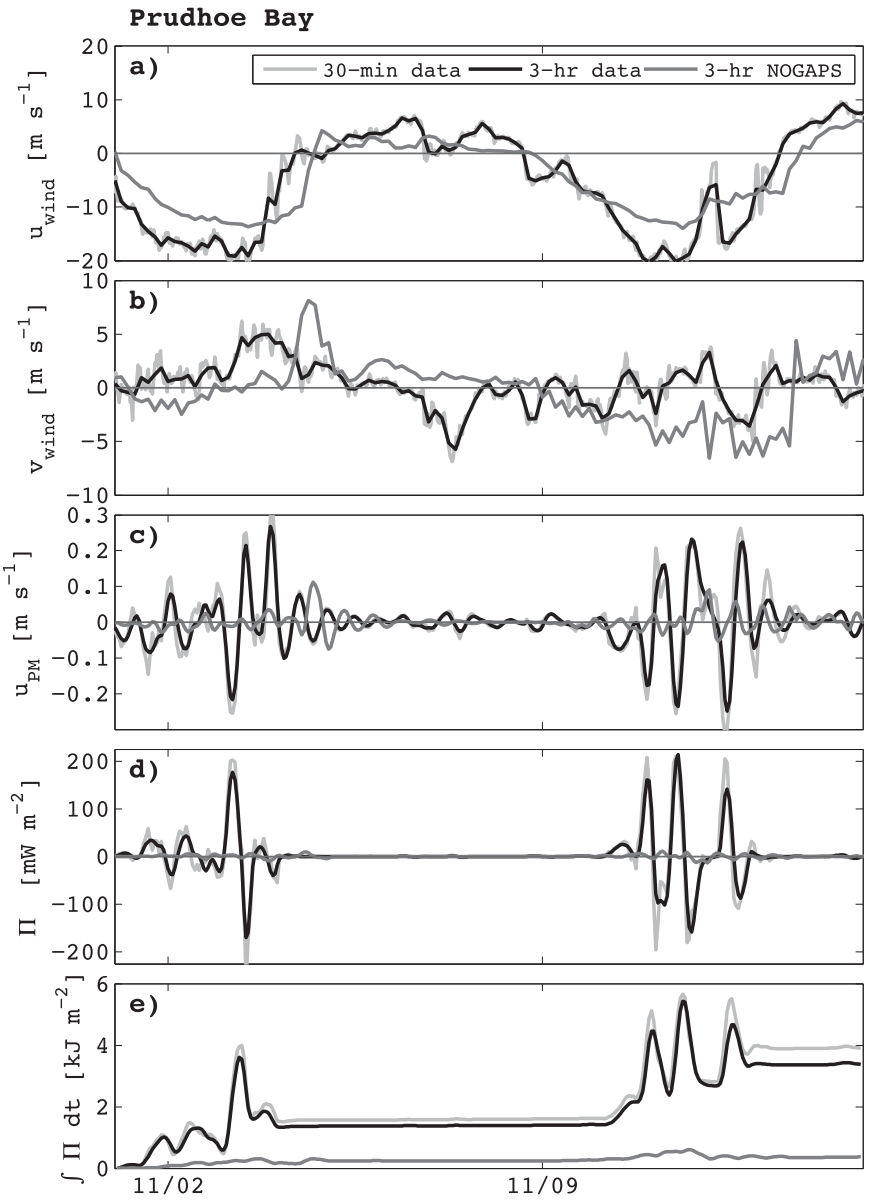

FIG. A1. Comparison of observed high-resolution 30-min winds (light gray lines) and 3-h bin-averaged winds (black) to 3-h NOGAPS reanalysis winds (medium gray) at Prudhoe Bay. (a) Zonal and (b) meridional wind speeds and (c) mixed layer inertial velocities, (d) wind energy flux to mixed layer inertial motions, and the (e) net energy transfer predicted by the slab model are shown.

also thank two anonymous reviewers for providing reviews that greatly improved the manuscript.

APPENDIX

Comparison of Wind Data Sources

The response of the Pollard–Millard slab model is sensitive to the temporal resolution of the input wind data. Previous analyses have suggested that the 3-h temporal resolution of reanalysis wind products is too sparse to force the Pollard–Millard slab model poleward of 50° due to decreasing inertial periods (D'Asaro 1985; Alford 2001). By comparing Navy Operational Global Atmospheric Prediction System (NOGAPS) reanalysis winds to high-resolution and subsampled wind data at Prudhoe Bay, it is confirmed that 3-h reanalysis winds do not currently accurately predict energy transfer from winds to inertial oscillations.

At Prudhoe Bay, the NOGAPS grid has zonal and meridional spatial resolutions of 18 and 55 km, respectively. The grid point closest to each station was chosen for this analysis. In situ winds are averaged into 30-min and 3-h bins to compare with NOGAPS data. Between the datasets, wind speeds match well at low frequencies but differ at higher frequencies (Figs. A1a,b). Surface velocities, fluxes, and net energy transfer predicted using in situ 30-min and 3-h binned wind data are similar (Figs. A1c–e). The closeness of the two predictions using in situ data suggest that high-frequency data averaged into 3-h bins can be used to accurately force the slab model and estimate mixed layer velocities. However, velocity, flux, and energy transfer calculated using the 3-h NOGAPS data is significantly different, having different magnitudes and phase from the in situ data. It is likely that the NOGAPS data do not fully resolve winds that are resonant at the local inertial frequency.

Similar analysis between in situ and NCEP North American Regional Reanalysis (NARR) winds at Point Barrow produce the same discrepancies (NCEP reanalysis data provided by the NOAA/OAR/ESRL PSD, Boulder, Colorado, from their website at http://www.esrl.noaa.gov/psd/). These discrepancies are likely due to the sparseness of in situ and satellite scatterometer data in the Arctic that is normally incorporated into the reanalysis product at lower latitudes, manifesting as noise at frequencies with periods shorter than 3 days that obscures the inertial signal. It is because of these inconsistencies that in situ winds at Prudhoe and Barrow are used to force the slab model. Close agreement between the results from the 1- and 3-h binned in situ data suggests a reanalysis product that resolves winds that are resonant at the local inertial frequency could be used to accurately predict mixed layer velocities with the slab model at higher latitudes, but currently NOGAPS and NARR reanalysis products cannot.

REFERENCES

Alford, M. H., 2001: Internal swell generation: The spatial distribution of energy flux from the wind to mixed layer near-inertial motions. *J. Phys. Oceanogr.,* **31,** 2359–2368, doi:10.1175/1520-0485(2001)031<2359:ISGTSD>2.0.CO;2.

——, and M. Whitmont, 2007: Seasonal and spatial variability of near-inertial kinetic energy from historical moored velocity records. *J. Phys. Oceanogr.,* **37,** 2022–2037, doi:10.1175/JPO3106.1.

Comiso, J. C., 2012: Bootstrap sea ice concentrations from Nimbus-7 SMMR and DMSP SSM/I-SSMIS, version 2. National Snow and Ice Data Center, Boulder, CO, digital media. [Available online at http://nsidc.org/data/docs/daac/nsidc0079_bootstrap_seaice.gd.html.]

——, C. L. Parkinson, R. Gersten, and L. Stock, 2008: Accelerated decline in the Arctic sea ice cover. *Geophys. Res. Lett.,* **35,** L01703, doi:10.1029/2007GL031972.

D'Asaro, E. A., 1985: The energy flux from the wind to near-inertial motions in the surface mixed layer. *J. Phys. Oceanogr.,* **15,** 1043–1059, doi:10.1175/1520-0485(1985)015<1043:TEFFTW>2.0.CO;2.

——, and M. D. Morehead, 1991: Internal waves and velocity fine structure in the Arctic Ocean. *J. Geophys. Res.,* **96,** 12 725–12 738, doi:10.1029/91JC01071.

——, and J. H. Morison, 1992: Internal waves and mixing in the Arctic Ocean. *Deep-Sea Res.,* **39** (Suppl. 2), S459–S484, doi:10.1016/S0198-0149(06)80016-6.

Dosser, H. V., L. Rainville, and J. M. Toole, 2014: Near-inertial internal wave field in the Canada basin from ice-tethered profilers. *J. Phys. Oceanogr.,* **44,** 413–426, doi:10.1175/JPO-D-13-0117.1.

Ekman, V. W., 1902: Om jordrotationens inverkan på vindströmmar i hafvet. *Nyt Mag. Naturvidensk.,* **40,** 37–64.

Fer, I., R. Skogseth, and F. Geyer, 2010: Internal waves and mixing in the marginal ice zone near the Yermak Plateau. *J. Phys. Oceanogr.,* **40,** 1613–1630, doi:10.1175/2010JPO4371.1.

Garrett, C., and W. Munk, 1975: Space-time scales of internal waves: A progress report. *J. Geophys. Res.,* **80,** 291–297, doi:10.1029/JC080i003p00291.

Gill, A. E., 1982: *Atmosphere–Ocean Dynamics.* Academic Press, 662 pp.

Guthrie, J. D., J. H. Morison, and I. Fer, 2013: Revisiting internal waves and mixing in the Arctic Ocean. *J. Geophys. Res.: Oceans,* **118,** 3966–3977, doi:10.1002/jgrc.20294.

Halle, C., and R. Pinkel, 2003: Internal wave variability in the Beaufort Sea during the winter of 1993/1994. *J. Geophys. Res.,* **108,** 3210, doi:10.1029/2000JC000703.

Hutchings, J. K., and I. G. Rigor, 2012: Role of ice dynamics in anomalous ice conditions in the Beaufort Sea during 2006 and 2007. *J. Geophys. Res.,* **117,** C00E04, doi:10.1029/2011JC007182.

——, P. Heil, A. Steer, and W. D. Hibler, 2012: Subsynoptic scale spatial variability of sea ice deformation in the western Weddell Sea during early summer. *J. Geophys. Res.,* **117,** C01002, doi:10.1029/2011JC006961.

Kendall, M. G., 1938: A new measure of rank correlation. *Biometrika,* **30,** 81–93, doi:10.2307/2332226.

Kowalik, Z., and A. Proshutinsky, 1994: The Arctic Ocean tides. *The Polar Oceans and Their Role in Shaping the Global Environment, Geophys. Monogr.,* Vol. 85, Amer. Geophys. Union, 137–158, doi:10.1029/GM085p0137.

Kunze, E., 1985: Near-inertial wave propagation in geostrophic shear. *J. Phys. Oceanogr.,* **15,** 544–565, doi:10.1175/1520-0485(1985)015<0544:NIWPIG>2.0.CO;2.

Large, W. G., and S. Pond, 1981: Open ocean momentum flux measurements in moderate to strong winds. *J. Phys. Oceanogr.,* **11,** 324–336, doi:10.1175/1520-0485(1981)011<0324:OOMFMI>2.0.CO;2.

Leaman, K. D., and T. B. Sanford, 1975: Vertical energy propagation of inertial waves: A vector spectral analysis of velocity profiles. *J. Geophys. Res.,* **80,** 1975–1978, doi:10.1029/JC080i015p01975.

Levine, M. D., 1990: Internal waves under the Arctic pack ice during the Arctic Internal Wave Experiment: The coherence structure. *J. Geophys. Res.,* **95,** 7347–7357, doi:10.1029/JC095iC05p07347.

——, C. A. Paulson, and J. H. Morison, 1985: Internal waves in the Arctic Ocean: Comparison with lower-latitude observations. *J. Phys. Oceanogr.,* **15,** 800–809, doi:10.1175/1520-0485(1985)015<0800:IWITAO>2.0.CO;2.

——, ——, and ——, 1987: Observations of internal gravity waves under the Arctic pack ice. *J. Geophys. Res.,* **92,** 779–782, doi:10.1029/JC092iC01p00779.

Martini, K. I., M. H. Alford, E. Kunze, S. M. Kelly, and J. D. Nash, 2011: Observations of internal tides on the Oregon continental slope. *J. Phys. Oceanogr.,* **41,** 1772–1794, doi:10.1175/2011JPO4581.1.

McPhee, M. G., 1978: A simulation of inertial oscillation in drifting pack ice. *Dyn. Atmos. Oceans,* **2,** 107–122, doi:10.1016/0377-0265(78)90005-2.

——, and L. H. Kantha, 1989: Generation of internal waves by sea ice. *J. Geophys. Res.,* **94,** 3287–3302, doi:10.1029/JC094iC03p03287.

Morison, J. H., C. E. Long, and M. D. Levine, 1985: Internal wave dissipation under sea ice. *J. Geophys. Res.,* **90,** 11 959–11 966, doi:10.1029/JC090iC06p11959.

Nansen, F., 1902: *The Oceanography of the North Polar Basin.* Longmans, Green, and Company, 427 pp.

Padman, L., and S. Erofeeva, 2004: A barotropic inverse tidal model for the Arctic Ocean. *Geophys. Res. Lett.,* **31,** L02303, doi:10.1029/2003GL019003.

——, A. J. Plueddemann, R. D. Muench, and R. Pinkel, 1992: Diurnal tides near the Yermak Plateau. *J. Geophys. Res.,* **97,** 12 639–12 652, doi:10.1029/92JC01097.

Partington, K., and C. Bertoia, 1999: Evaluation of Special Sensor Microwave/Imager sea-ice products. U.S. Department of Commerce Paper 58, 3 pp.

Pickart, R. S., L. M. Schulze, G. W. K. Moore, M. A. Charette, K. R. Arrigo, G. van Dijken, and S. L. Danielson, 2013a: Long-term trends of upwelling and impacts on primary productivity in the Alaskan Beaufort Sea. *Deep-Sea Res. I,* **79,** 106–121, doi:10.1016/j.dsr.2013.05.003.

——, M. A. Spall, and J. T. Mathis, 2013b: Dynamics of upwelling in the Alaskan Beaufort Sea and associated shelf–basin fluxes. *Deep-Sea Res. I,* **76,** 35–51, doi:10.1016/j.dsr.2013.01.007.

Pinkel, R., 2005: Near-inertial wave propagation in the western Arctic. *J. Phys. Oceanogr.,* **35,** 645–665, doi:10.1175/JPO2715.1.

Plueddemann, A. J., R. Krishfield, T. Takizawa, K. Hatakeyama, and S. Honjo, 1998: Upper ocean velocities in the Beaufort Gyre. *Geophys. Res. Lett.,* **25,** 183–186, doi:10.1029/97GL53638.

Pollard, R. T., and R. C. Millard, 1970: Comparison between observed and simulated wind-generated inertial oscillations. *Deep-Sea Res. Oceanogr. Abstr.,* **17,** 813–816, doi:10.1016/0011-7471(70)90043-4.

Rainville, L., and R. A. Woodgate, 2009: Observations of internal wave generation in the seasonally ice-free Arctic. *Geophys. Res. Lett.,* **36,** L23604, doi:10.1029/2009GL041291.

Rothrock, D. A., 1975: The energetics of the plastic deformation of pack ice by ridging. *J. Geophys. Res.,* **80,** 4514–4519, doi:10.1029/JC080i033p04514.

Schulze, L., and R. Pickart, 2012: Seasonal variation of upwelling in the Alaskan Beaufort Sea: Impact of sea ice cover. *J. Geophys. Res.,* **117,** C06022, doi:10.1029/2012JC007985.

Shcherbina, A. Y., D. Rudnick, and L. Talley, 2005: Ice-draft profiling from a bottom-mounted ADCP data. *J. Atmos. Oceanic Technol.,* **22,** 1249–1266, doi:10.1175/JTECH1776.1.

Spall, M. A., R. S. Pickart, P. S. Fratantoni, and A. J. Plueddemann, 2008: Western Arctic shelfbreak eddies: Formation and transport. *J. Phys. Oceanogr.,* **38,** 1644–1668, doi:10.1175/2007JPO3829.1.

Stroeve, J., M. Serreze, M. Holland, J. Kay, J. Malanik, and A. Barrett, 2012: The Arctic's rapidly shrinking sea ice cover: A research synthesis. *Climatic Change,* **110,** 1005–1027, doi:10.1007/s10584-011-0101-1.

Thorndike, A. S., and R. Colony, 1982: Sea ice motion in response to geostrophic winds. *J. Geophys. Res.,* **87,** 5845–5852, doi:10.1029/JC087iC08p05845.

Toole, J. M., M. L. Timmermans, D. K. Perovich, R. A. Krishfield, A. Proshutinsky, and J. A. Richter-Menge, 2010: Influences of the ocean surface mixed layer and thermohaline stratification on Arctic sea ice in the central Canada basin. *J. Geophys. Res.,* **115,** C10018, doi:10.1029/2009JC005660.

Weingartner, T. J., R. S. Pickart, and M. A. Johnson, 2010: *Recommended Physical Oceanographic Studies in the Alaskan Beaufort Sea.* U.S. Department of the Interior, Minerals Management Service, Alaska OCS Region, 90 pp.